INVESTIGATION OF THE ANOMALOUS QUANTUM TRANSPORT IN MULTICHANNEL SYSTEMS

A Thesis Submitted to
the Graduate School of
İzmir Institute of Technology
in Partial Fulfillment of the Requirements for the Degree of

DOCTOR OF PHILOSOPHY

in Photonic Science and Engineering

by
Hazan ÖZKAN

July, 2024
İZMİR

We approve the thesis of **Hazan ÖZKAN**

Examining Committee Members:

Assoc. Prof. Dr. Sevilay SEVİNÇLİ
Department of Photonics, İzmir Institute of Technology

Assoc. Prof. Dr. Özgür ÇAKIR
Department of Physics, İzmir Institute of Technology

Assoc. Prof. Dr. Seymur JAHANGİROV
Department of Materials Science and Nanotechnology, UNAM

Prof. Dr. Alev Devrim GÜÇLÜ
Department of Physics, İzmir Institute of Technology

Assoc. Prof. Dr. Ümit AKINCI
Department of Physics, Dokuz Eylül University

04/07/2024

Assoc. Prof. Dr. Sevilay SEVİNÇLİ
Supervisor, Department of Photonics
İzmir Institute of Technology

Prof. Dr. Hâldun SEVİNÇLİ
Co-Supervisor, Department of Physics,
Bilkent University

Prof. Dr. Canan VARLIKLI
Head of the Department of
Photonics

Prof. Dr. Mehtap EANES
Dean of the Graduate School

ACKNOWLEDGMENTS

I would like to thank my advisors, Prof. Dr. Hâldun SEVİNÇLİ and Assoc. Prof. Dr. Sevilay SEVİNÇLİ for the guidance and advice they have provided throughout my PhD period. It was an honor and a privilege to be supervised by them.

I would like to thank my thesis committee members, Assoc. Prof. Dr. Özgür ÇAKIR, Assoc. Prof. Dr. Seymur JAHANGİROV, Prof. Dr. A. Devrim GÜÇLÜ and Assoc. Prof. Dr. Ümit AKINCI for their valuable feedback and their contributions.

Working with our group members, Dr. Gizem KURT and Dr. Mustafa POLAT, was a great pleasure; I would like to thank them for their friendship and support.

I would like to thank all my friends in İYTE and give special thanks to Semih FİLİZ, Begüm YAVAŞ AYDIN and Dr. Nahit POLAT for their friendship, support, and encouragement during the most challenging times of my PhD period.

Finally, I would like to thank my family for their encouragement and endless support during my life. They have shown me unconditional love in all situations and made it possible to this journey.

This work was supported by The Scientific and Technological Research Council of Turkey TÜBİTAK under Project No. 119F353.

ABSTRACT

INVESTIGATION OF THE ANOMALOUS QUANTUM TRANSPORT IN MULTICHANNEL SYSTEMS

In this study, the anomalous quantum transport behavior without Levy-type disorder is investigated in multichannel systems. The transmission properties of the systems are calculated by using tight-binding Hamiltonians and Landauer formalism. The mode-matching method is used to investigate the transmission properties of the channels individually. The calculations, at first, are performed for a two-channel toy model in a correlated fashion. This method aims to recognize the general behavior of anomalous diffusion regardless of the system's structure. Then, we focus on realistic systems. Quasi-one-dimensional ribbons of graphene and those of a quartic dispersion material,i.e., nitrogen, are studied in the presence of disorder. It is observed that since defects are introduced only at the edges, the scatterings are more pronounced at the modes where the edge contributions are more dominant. As a result, the average transmission with an increasing length shows heavy tail distribution. This behavior is a characteristic property of anomalous diffusion. The transport characteristics of these systems are investigated in detail by performing a mode-resolved analysis. Moreover, quantum shot noise and Fano factor are calculated for the investigated systems. It is suggested that the Fano factor can be used as an indicator for anomalous diffusion in these systems. We conclude that anomalous diffusion can be realized in multichannel systems without Levy-type disorder and in the presence of correlated disorder, which can drive channels into different transport regimes.

Lastly, by increasing the length of the system, transport behavior is investigated for the localization regime. In this regime, the relation between the geometric average of the transmission and the system length showed linear dependency, indicating normal localization. Since the multichannel mechanism was suppressed, anomalous behavior disappeared at large scales. This result is consistent with the diffusion part. Because, in our models, anomalies resulted from the multichannel structure.

ÖZET

ÇOK KANALLI SİSTEMLERDE ANORMAL KUANTUM TAŞINIMININ İNCELENMESİ

Bu çalışmada, çok kanallı sistemlerde Levy düzensizliklerinin olmadığı durumlarda kuantum davranışları incelendi. Sistemlerin taşınım özellikleri sıkı-bağ Hamiltonyeni ve Landauer formalizmi kullanılarak hesaplandı. Kanalların taşınım özelliklerini ayrı olarak inceleyebilmek için ise mod-eşleştirme yöntemi kullanıldı. Hesaplamalar ilk olarak iki-kanallı oyuncak modelde Anderson düzensizliği uygulanarak gerçekleştirildi. Bu model sistemin yapısından bağımsız olarak anormal difüzyonun genel davranışını anlamayı amaçlar. Daha sonra gerçekçi sistemlere odaklanıldı. Yarı-tek boyutlu grafen ve kuartik dağılım gösteren, nitrojen gibi, malzemelerin şeritlerinde düzensizlikler çalışıldı. Düzensizlikler sadece kenarlara uygulandığı için saçılımların kenar katkılarının baskın olduğu modlarda daha belirgin olduğu gözlemlendi. Sonuç olarak, ortalama taşınım artan uzunluğa bağlı olarak anormal difüzyonun karakteristik özelliği olan ağır kuyruklu dağılım gösterdi. Bu sistemlerin taşınım karakteristikleri mod-çözümleme analizi uygulanarak detaylı olarak incelendi. Ayrıca, incelenen sistemler için kuantum saçma gürültüsü ve Fano faktörü hesaplandı. Fano faktörünün bu sistemlerde belirleyici olarak kullanılabileceği öne sürüldü. Kanalları farklı difüzyon rejimlerine sokan birbiriyle bağlantılı düzensizliklerin varlığında, Levy tarzı dağılım olmadan da çok kanallı sistemlerde anormal difüzyon meydana gelebileceği sonucuna varıldı.

Son olarak, sistemin uzunluğu arttırılarak taşınım davranışı lokalizasyon rejiminde incelendi. Bu rejimde, taşınımın geometrik ortalaması ve sistem uzunluğu birbiriyle lineer olarak ilişkilidir ve normal lokalizasyonu işaret eder. Sistemin uzunluğu arttırıldığında çok kanallılıkla ortaya çıkan mekanizma baskılandığından, anormal davranış kaybolur. Bu durum difüzyon kısmındaki sonuçlarla tutarlıdır çünkü modellerimizde anormallikler çoklu kanal yapısından kaynaklanmaktadır.

To my family ...

TABLE OF CONTENTS

LIST OF FIGURES

Figure **Page**

LIST OF SYMBOLS

SYMBOL	EXPLANATION
λ_{mfp}	Mean Free Path
λ_{sp}	Spread Length
ξ_{loc}	Localization Length
M	Number of Modes
T	Transmission
G	Conductance
t	Transmission Matrix
$tt^{\dagger}$	Transmission Matrix Product
$\mathcal{T}_N$	Transmission Eigenvalues
S	Shot Noise
F	Fano Factor
R_4	Four-Probe Resistance

CHAPTER 1

INTRODUCTION

Transport theory investigates the motion of particles or waves. Each type of transport process has characteristic behaviors and can be analyzed by consulting suitable physical principles. In this study, when we mention transport, we refer to the electronic transport mostly encountered in nanodevices where the quantum mechanical effects become crucial.

The transport mechanism is closely associated with the random walk motion. This process is observed in various phenomena in nature. The origin of this process is based on the fact that particles and waves travel with random trajectories. The random walk was first discovered by botanist Robert Brown in 1827 at the motion of pollen grains in a fluid (Brown, 1828). The mathematical description of this motion was first explained by Thorvald N. Thiele in 1880 (Lauritzen, 2002). Over time, including Albert Einstein in 1905, many scientists have contributed to understanding the unrevealed mechanism of this concept (Einstein, 1956).

The mathematics behind the Brownian motion can be used to explain the diffusion of light and heat. Various experimental studies have been conducted on the Brownian motion, or in other words, normal diffusion. However, in addition to normal diffusion, the Levy transport is another observed phenomenon in nature. The Levy transport generally includes the Levy walk, a particular type of random walk based on the power law distribution (Uchaikin and Zolotarev, 2011). This type of diffusion is generally observed in photonic crystals (Koenderink and Vos, 2005; Le Thomas et al., 2009; Rousseau and Felbacq, 2017), lasers (Lepri et al., 2007; Rocha et al., 2020), fluid dynamics (Pasmanter, 1988; Osborne and Caponio, 1990) , economics (Mantegna and Stanley, 1995; Miranda and Riera, 2001) , human behavior (Baronchelli and Radicchi, 2013), travel patterns (Brockmann et al., 2006), and, most generally, in chaotic systems (Iomin and Zaslavsky, 2002; Klafter et al., 1995; Solomon et al., 1994).

The Levy transport has been the subject of several studies because it is easily encountered in nature. The study of Davis and Marshak (Davis and Marshak, 1997) belongs to this type of diffusion, which investigates photon transport in a cloudy atmosphere and can be considered the most well-known. According to this study,

the optical densities of the clouds vary depending on the cloud types, so it is an excellent example of a natural scattering medium. The trajectories of the solar photons in these areas show random walks, and the diversity of the properties of these clouds has a crucial effect on this process. Based on the optical density of clouds, photons can transmit slower or may even trapped in some areas. When the inhomogeneity of the region increases, reflectivity decreases, and the model becomes much more transmissive. Because of all these properties, analyzing the system with the power law statistics is much more suitable for this model. Another study that motivates this research has the theoretical and experimental background about the Levy transport of light (Barthelemy et al., 2008). This study was performed with glass microspheres. The critical point related to Levy transport is the diameter of the microspheres. These diameters were arranged according to the Levy distribution. Then, they were introduced to the solution, which included titanium dioxide inside the liquid sodium silicate. In this study, the size of the microsphere diameters has an essential effect on the scattering and the light path. According to their observations, after using the He-Ne laser, they observed fluctuations in transmission since the light paths are not constant during the scatterings. This outcome is crucial because it provides experimental evidence of the characteristics of Levy transport.

On the other hand, some examples are based on numerical quantum mechanical calculations. In 1998, a study was published investigating the Levy transport in the square lattice by using Anderson disorder (Leadbeater et al., 1998). However, unlike our models, this study considers the magnetic field and investigates its effects on the deflection of Levy flights. Recently, a new study was published, which is more related to our research area based on the building Levy glass structure (Fonseca et al., 2023). This study uses graphene nanoribbons as a material consisting of a multichannel structure similar to our models. However, the physics behind this research is different than ours. Here, on the surface of the nanoribbons, the tunable spin-orbit regions are generated as the shape of circular regions. The diameter of these areas is arranged according to the power law distribution. Their results show that the spin polarizations in these clusters were observed for the superdiffusive regime. These results are significant, especially in spintronic applications like spin filters.

This thesis investigated the electronic quantum transport in the zigzag graphene and quartic nanoribbons under edge disorder. As different from the literature, we did not introduce Levy distribution or magnetic field to our systems, or we did not

consider the spin-orbit effects. Instead, we focus on the multichannel structures of our systems. While performing our calculations, we randomly introduced the disorders to the edge atoms. To model the systems, we used a tight-binding Hamiltonian. After constructing the structures, we calculated transmission using the Green's function method. Then, we obtained our results by taking the ensemble averages over different disorder configurations. According to our results, under the edge disorder, graphene and quartic nanoribbons show anomalous diffusion. We also used the mode-matching method to understand the reason behind this behavior. Since we focused on the multichannel mechanism, the mode-matching method gave us a new perspective by analyzing the transport of the channels as individuals. After that, we increased the system length and performed our calculations in the localization regime. According to our results, the multichannel mechanism was suppressed at these scales, and we observed normal localization.

This thesis's first chapter includes a short review of the basic concepts of electronic quantum transport. Chapter 2 discusses the methods we used during our calculations, including the Greens function method, the mode matching method, and some numerical techniques to gain from the speed and memory. Chapter 3 explains the steps we used while constructing our models and includes the transport calculations with their interpretations. The final chapter is a conclusion that includes a summary of our research.

1.1. Characteristic Length Scales

There are some fundamental length scales mainly used during the transport process, including the Fermi wavelength λ_F, the phase coherence length λ_ϕ, the mean free path λ_{mfp} and the localization length ξ_{loc}.
The Fermi wavelength has a crucial role in understanding the behaviors of the electrons in the material and is related to the inverse of the wave vector k_F as

$$\lambda_F = 2\pi/k_F. \tag{1.1}$$

The phase coherence length, λ_ϕ, gives a clue to understanding the quantum mechanical effects on transport. This characteristic length can be defined as the

average distance of electrons during the travel before scattering and losing their quantum mechanical phase. The phase coherence length can be calculated from

$$\lambda_\phi = v_F \tau_\phi \tag{1.2}$$

where τ_ϕ is the phase coherence time and v_F is the Fermi velocity.

The mean free path λ_{mfp}, on the other hand, can be defined as the average distance before the particle scatters and changes its direction. We mainly used this length scale as a characteristic parameter during our calculations since we mostly worked on the diffusion regime. Regarding a type of collision, the mean free path can be elastic or inelastic. The critical difference between the inelastic and elastic collision is the energy exchange. In the elastic collisions, there are no energy exchanges. They generally formed due to the defects in the lattice, as in our models. The elastic mean free path can be calculated from

$$\lambda_{mfp} = v_F \tau_{el} \tag{1.3}$$

where τ_{el} is time taking between the elastic scatterings.

The last scale is the localization length ξ_{loc}. The localization length of the system is related to the mean free path and indicates the length where diffusion decreases or even vanishes. If the $\lambda_\phi < \xi_{loc}$, the electrons loose phase coherence. As a result, interference effects disappear, and the system behaves classically. However, for large λ_ϕ, electrons coherently move in closed paths resulting in bound states (Torres et al., 2014).

1.2. Quantum Transport Regimes

This section includes the roles of the characteristic length scales while determining the transport regimes. These are Ballistic, Diffusion, and Localization regimes.

1.2.1. Ballistic and Diffusion Regimes

The main difference between the ballistic regime and the diffusive regime is the relation between the length of the system L and the mean free path λ_{mfp}. By using the characteristic length scales, the transport regimes can be determined. Figure 1.1 is an illustration of the ballistic and diffusion regime.

In the ballistic regime, the system size is smaller than the mean free path. Electrons travel through a conductor without scattering. In the diffusion regime, on the other hand, the mean free path is smaller than the system size in this regime. As a result, the electrons travel through a conductor by doing random walks while experiencing scattering. In addition to these two regimes, there is a quasi-ballistic regime, which has properties similar to these two regimes. The system size and the mean free path can be comparable in the quasi-ballistic regime.

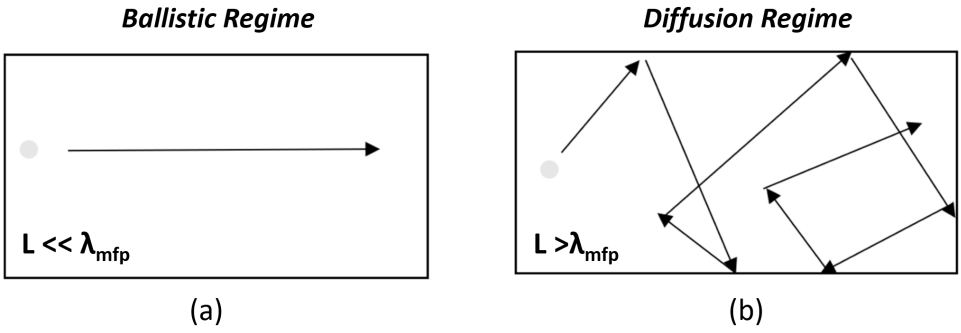

Figure 1.1. An illustration of (a) ballistic regime (b) diffusion regime

We used the transmission formula to investigate the relation between the transmission and the system length. This formula can be derived considering a system that includes two scattering centers. These scattering centers can represent defects in the material.

Figure 1.2 illustrates a system with two scattering centers where the electron comes from the left side. The electron moves through the scattering centers with a reflection and transmission probability R_1, R_2 and T_1, T_2.

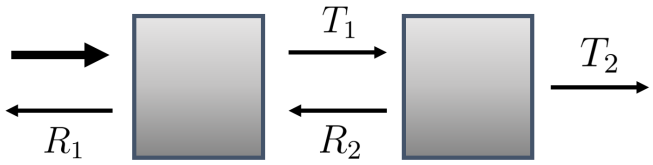

Figure 1.2. The illustration of a system consists of two scattering centers. The electron comes from the left side and moves through the scattering centers with a transmission probabilities T_1, T_2, and reflection probabilities R_1, R_2.

For this system, the possible outcomes can be written as

$$T_{12} = T_1T_2 + T_1R_1R_2T_2 + T_1R_1^2R_2^2T_2 + ... \tag{1.4}$$

where T_{12} is the probability of an electron transmitting through both scattering centers. The possible outcomes have two transmission probabilities: T_1 for the first center and T_2 for the second center. In addition, these outcomes consist of an even number of reflection probabilities R_1 and R_2.
By using the expansion

$$1 + x + x^2 + ... = \frac{1}{1-x}, \tag{1.5}$$

the result can be simplify as

$$T_{12} = \frac{T_1T_2}{1 - R_1R_2}. \tag{1.6}$$

Since $R_1 = 1 - T_1$ and $R_2 = 1 - T_2$, Equation 1.6 becomes

$$\frac{T_1T_2}{1 - R_1R_2} = \frac{T_1T_2}{(T_1 + T_2) - T_1T_2}. \tag{1.7}$$

Therefore,

$$\frac{1}{T_{12}} = \frac{T_1 + T_2}{T_1T_2} - 1 = \frac{1}{T_1} + \frac{1}{T_2} - 1. \tag{1.8}$$

From the Equation 1.8, R_{12}/T_{12} can be obtained as

$$\frac{R_{12}}{T_{12}} = \frac{1}{T_{12}} - 1 = \frac{1}{T_1} - 1 + \frac{1}{T_2} - 1 = \frac{1-T_1}{T_1} + \frac{1-T_2}{T_2}. \tag{1.9}$$

For N identical scattering centers, each having transmission probability T, Equation 1.9 can be written as

$$\frac{1-T_N}{T_N} = \frac{N(1-T)}{T} \tag{1.10}$$

where T_N indicates the transmission probability of N identical scattering center and can be calculated from

$$T_N = \frac{T}{\rho L(1-T)+T}. \tag{1.11}$$

Here, L is the length of the system, and ρ is the linear density of scattering center. If the term $T/\rho(1-T)$ in the equation is defined as λ_{mfp}, the transmission probability in terms of the system length can be written as

$$T = \frac{\lambda_{mfp}}{L+\lambda_{mfp}}. \tag{1.12}$$

Here, λ_{mfp} indicates a constant called mean free path. When the length of the system equals the mean free path,the transmission probability becomes 1/2. In the case of M number of modes, the equation becomes

$$T = \frac{M}{1+(L/\lambda_{mfp})} \tag{1.13}$$

According to this equation, transmission is inversely proportional to the system length and obeys Ohm's Law (Datta, 1997, 2005). This behavior can be confirmed by using the definition of resistance. According to Ohm's law, the relation between the potential difference and the current shows linear behavior. The potential difference can be calculated from

$$V = IR \tag{1.14}$$

where V is the potential difference, I is the current and R is the resistance of the system. After applying the potential difference to a two-dimensional system, for

example, to a wire, the current can be obtained from

$$I = \frac{\sigma A V}{L}. \tag{1.15}$$

Here, $L/\sigma A$ indicates resistance where A is the cross-sectional area, and σ is the conductivity. This definition shows that resistance and the system length are linearly dependent ($R \propto L$). Since the conductance and resistance are inversely proportional, the conductance decreases depending on the system length ($G \propto 1/L$). At zero temperature, the relation obtained for conductance can also be used for transmission ($T \propto 1/L$). However, this classical behavior is only observed for normal diffusion where $\alpha = 2$.

In this case, the system shows normal diffusion and includes Gaussian random walk. However, Gaussian random walk is just a particular type of random walk. Therefore, in our calculations, we need a more general transmission formula. By using some statistical concepts, such as the characteristic function and the probability density function (PDF), it is possible to understand the link between random walk motion and transmission.
The general form of the symmetric distributions can be represented as

$$\hat{\rho}_{\alpha}^{ch}(c,k) = e^{-c|k|^{\alpha}}. \tag{1.16}$$

This term is also called characteristic function in statistics. Here, α is a crucial parameter to determine the type of the distribution. On the other hand, c in the equation specifies the tail of the distribution.

The Fourier transform of the characteristic function gives the probability density functions (PDF). Both PDF and characteristic functions have essential roles in transport. Using the characteristic function is generally preferred when analyzing the distributions, such as considering its mean and variance; the PDF, on the other hand, gives a visual solution; for example, it is better to see where data is concentrated. The probability density functions take their name according to the α values inside their equation. If $\alpha = 2$ the Fourier transform of this characteristic function gives Gaussian PDF. For another case, if $\alpha = 1$ PDF takes the name Lorenztian function. However, in other cases, these distributions do not have analytical solu-

tions (Uchaikin and Zolotarev, 2011). At these ranges, asymptotic limits must be considered.

For large x expansion

$$P_\alpha(c,x) \approx \frac{c}{\mid x \mid^{1+\alpha}} \tag{1.17}$$

which shows heavy tail distribution (Buldyrev et al., 2001; Barthelemy et al., 2008).

The situation we encountered in the transmission calculation is analogically similar to this concept. There are various cases where the transmission is linearly dependent on length. However, it does not always have to be like that. By taking into account these other possibilities, the literature uses a more general α dependent transmission equation for diffusion, which is (Barthelemy et al., 2008). The role of the α in the equation is similar to the version used in statistics.

$$T = \frac{M}{1 + (L/\lambda_{sp})^{\frac{\alpha}{2}}}. \tag{1.18}$$

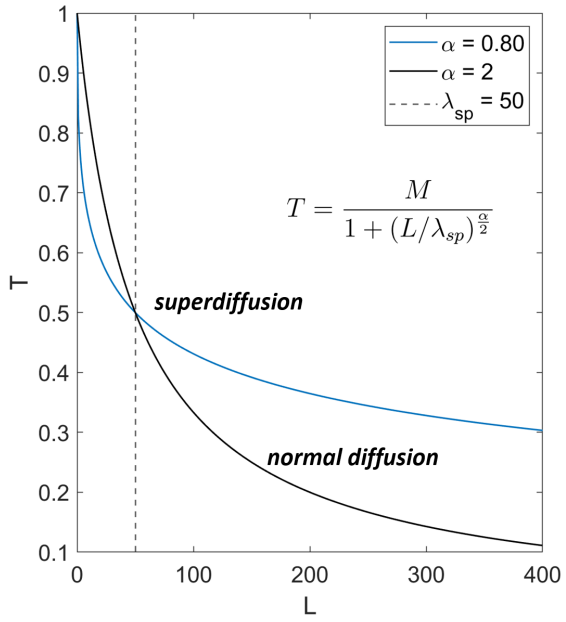

Figure 1.3. Comparison of the superdiffusion and normal diffusion depending on α values. During calculations, the spread length, λ_{sp}, is 50, and the number of modes, M, is 1 for both cases.

Figure 1.3 shows the transmission length dependence for different α. Transmission values obtained from Equation 1.16. where the spread length, λ_{sp}, and the number of modes are chosen as 50 and 1, respectively. According to this figure, In the case of $\alpha = 2$, the system shows normal diffusion, including Gaussian statistics. On the other hand, $\alpha < 2$ shows superdiffusion and decays faster than the normal diffusion case.

1.2.2. Localization Regime

According to Einstein, if the system exhibits a random walk, the diffusion equation is enough to explain the process. However, in 1958, Anderson proved that this statement is only valid for some cases (Anderson, 2010). Anderson suggests that random walks have a memory when dealing with quantum particles, and the interference effects should be considered. As a result of that, for an infinitely long time with a strong disorder, this process may result in localization.

In the case of the random disordered potential V the Schrödinger equation can be written as

$$-\frac{\hbar}{2m}\nabla^2\Psi(r) + V(r)\Psi(r) = E\Psi(r). \tag{1.19}$$

Depending on the relation between the energy and the potential, two different scenarios can be mentioned.

If $E > V$, the solution of the equation gives unbound states. These states represent extended states such as free particle solutions.

$$|\Psi(r)|^2 \propto L^{-d} \tag{1.20}$$

where d is the dimension of the system, and L is the size of the system.

If $V > E$, on the other hand, the solution of the equation gives bound states with discrete energy spectra. Bound states represent localized states.

$$|\Psi(r)|^2 \propto e^{-r/\xi_{loc}} \tag{1.21}$$

ξ_{loc} is the localization length (Abrahams, 2010). The transmission function, in the

logarithmic form, can be represented in the localization regime as (Fernández-Marín et al., 2012)

$$\langle -lnT \rangle \propto \begin{cases} 1 \leq \gamma < 2, & L(\text{Linear}) \\ 0 < \gamma < 1, & L^{\gamma}(\text{Power Law}) \end{cases}$$

In the literature, in addition to the standard localization, there are several studies related to anomalous localization (Méndez-Bermúdez et al., 2016; Amanatidis et al., 2017; Fernández-Marín et al., 2012; Zakeri et al., 2015).

1.3. Landauer Formalism

The Landauer formalism is a convenient way to describe quantum transport, including scattering effects. Landauer introduced this theory first in 1957 for metallic conductors (Landauer, 1957). Then, in 1970, this theory extended to one-dimensional lattices (Landauer, 1970). After that, in 1986, Büttiker generalized the formula for multi-lead systems (Büttiker, 1986).

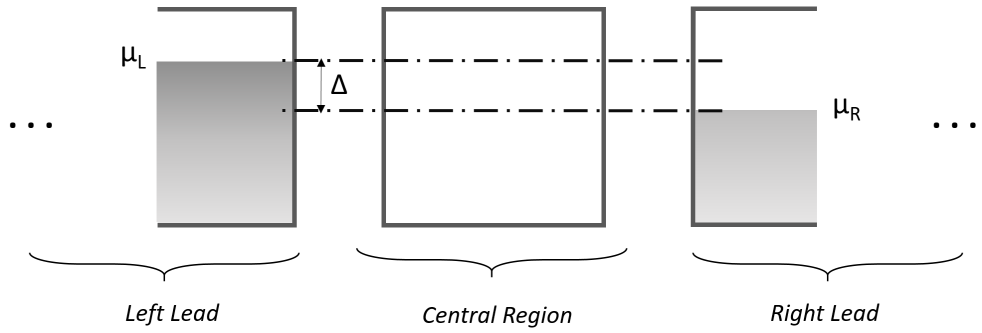

Figure 1.4. The illustration of the tripartite system consists of the central region connected with semi-infinite leads with both ends. The differences between the chemical potentials of the left lead μ_L and the right lead μ_R give rise to current.

This formalism considers a system connected to two semi-infinite periodic reservoirs with both ends, as represented in Figure 1.4. Each reservoir has its chemical potential μ, temperature, and Fermi function f. Electrons are injected from the leads

and move through the system. They can also be scattered back to the reservoirs. The difference between the chemical potentials μ_L and μ_R of the reservoirs indicated with Δ gives rise to the current in the system.

The total current can be calculated from the integration of the difference between Fermi levels of the reservoirs multiplied by the transmission amplitude $T(E)$ and can be written as

$$I = \frac{2e}{h} \int dE[f^L(E, \mu_L) - f^R(E, \mu_R)]T(E) \tag{1.23}$$

where $f^L(E, \mu_L)$ and $f^R(E, \mu_R)$ are Fermi distribution functions of the left and right lead, respectively. This equation is the most general form of the Landauer formalism and is called the two-terminal formula (Torres et al., 2014).

For the finite temperature case, the conductance becomes

$$G = \frac{2e^2}{h} \int dE T(E) \Big(-\frac{\partial f}{\partial E} \Big). \tag{1.24}$$

At zero temperature,

$$\Big(-\frac{\partial f}{\partial E} \Big) = \delta(E - E_F) \tag{1.25}$$

where E_F stands for the Fermi energy. Then, conductance can be calculated from

$$G = \frac{2e^2}{h} T(E_F). \tag{1.26}$$

If the system consists of M number of modes, the equation becomes

$$G = \frac{2e^2}{h} M T(E_F). \tag{1.27}$$

By using the definition of the transmission probability in terms of the mean free path equation can also be written as

$$G = \frac{e^2}{h} M \frac{\lambda}{\lambda + L}. \tag{1.28}$$

Therefore, the two probe resistance becomes

$$R = \frac{h}{e^2 M} + \frac{h}{e^2 M}\frac{L}{\lambda} \tag{1.29}$$

where the h/e^2 is the contact resistance for perfect wire. In Equation 1.29, resistance consists of two terms. The first term indicates interface resistance, while the second one is device resistance, or in other words, the four-probe resistance. Therefore, R_4 which is called the devices resistance becomes

$$R_4 = \frac{1}{M}\frac{L}{\lambda}. \tag{1.30}$$

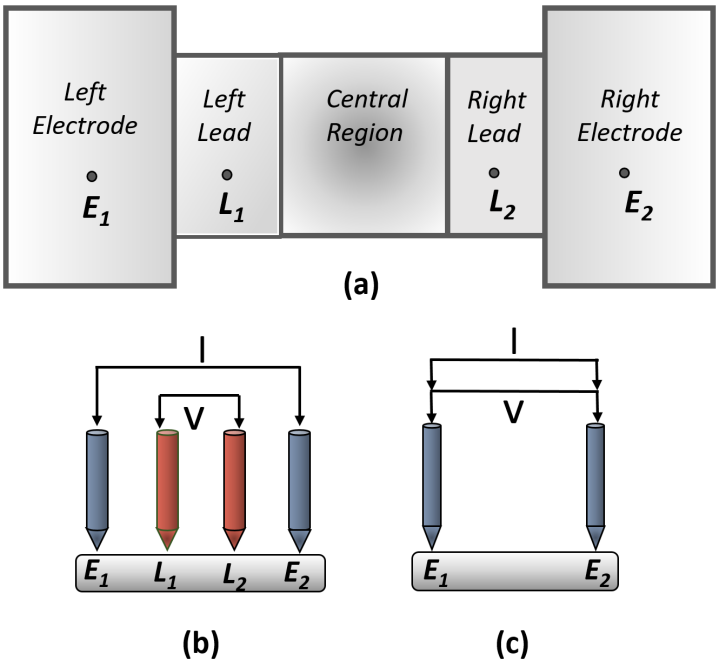

Figure 1.5. Illustration of the (a) measurement points on the total system (b) a four-probe resistance (c) a two-probe resistance

The main difference between the two-probe and the four probe equations is that the point where the voltage is applied. In the case of four-probe system,

measurements are taken from inside the leads, while for two-probe case, inside the electrodes. In a system like that, the leads take a role as waveguides of electrons by connecting them with the central region (Ryndyk et al., 2016).

Figure 1.5 is the illustration of this process. In the four-probe resistance, the current is applied to the system from the points L_1 and L_2. In the two-probe resistance on the hand, both current and voltage are applied from the same points, which are E_1 and E_2.

1.4. Scattering Matrix

The characteristic properties of the scattering process are determined by the scattering matrix (S matrix). There is a strong relation between the S matrix and the transport process. S matrix provides a direct way to calculate the transmission eigenvalues, which is crucial for transport calculations.

We can first consider a sample with one scattering center to understand the scattering mechanism, represented in Figure 1.6. According to this figure, if a wave is coming from the left, it can be either transmitted to the left with a transmission amplitude t or reflected to the right with a reflection amplitude r. A similar process can be applied to the right-coming wave whose transmission and reflection amplitudes become t' and r', respectively. These outcomes can be represented as the elements of the S matrix.

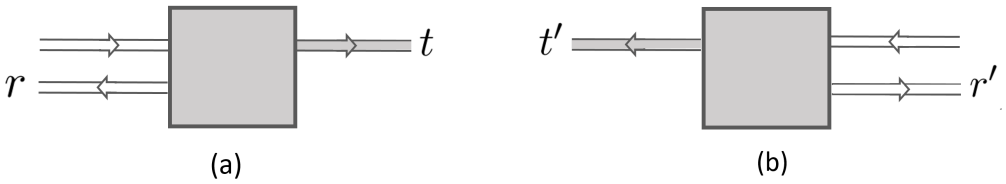

Figure 1.6. Illustration of the system with one scattering center and a single channel where waves come from (a) the left and (b) the right. t,t' and r,r' represent transmission and reflection amplitudes, respectively.

The scattering matrix for this system can be represented generally as

$$S = \begin{pmatrix} s_{LL} & s_{LR} \\ s_{RL} & s_{RR} \end{pmatrix} = \begin{pmatrix} r & t' \\ t & r' \end{pmatrix} \tag{1.31}$$

S matrix provides a relation between the incoming and outgoing states of the system. In a single-channel case, outcomes are directly related to amplitudes. Since the S matrix is unitary, the total probability is always conserved.

$$SS^{\dagger} = S^{\dagger}S = 1. \tag{1.32}$$

Their absolute squares give the transmission and reflection probabilities.

$$\begin{aligned} T &= \mid t \mid^2 \quad T' = \mid t' \mid^2 \\ R &= \mid r \mid^2 \quad R' = \mid r' \mid^2 \end{aligned} \tag{1.33}$$

In the multichannel case, which is illustrated in Figure 1.7, similar steps can be followed. However, the possible outcomes will be increased depending on the number of channels. Therefore, determining and working on one specific channel will be much easier. Figure 1.6 shows the possible outcomes of an electron coming from the left in the mth transport channel.

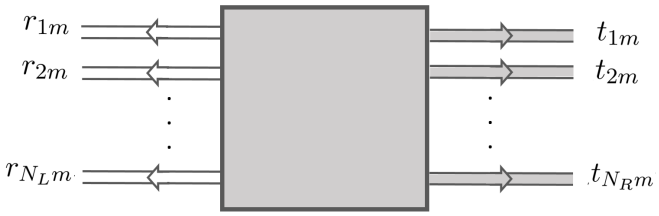

Figure 1.7. Illustration of the scattering mechanism in a multi-channel system. Transmission and reflection amplitudes indicated for the electron coming from the left in the mth channel. The total number of channels is represented with N_L and N_R for the left and right sides, respectively.

In that case, the elements of the S matrix consist of the reflection $(\hat{r}, \hat{r'})$ and the transmission matrices $(\hat{t}, \hat{t'})$, instead of the amplitudes. In general form, it can be represented as

$$S = \begin{pmatrix} \hat{r} & \hat{t'} \\ \hat{t} & \hat{r'} \end{pmatrix} \tag{1.34}$$

The dimension of the S matrix is determined in terms of the total number of channels, which is equal to $(N_L + N_R) \times (N_L + N_R)$ in this case.
From the unitary property

$$SS^{\dagger} = S^{\dagger}S = \mathbb{1}. \tag{1.35}$$

Therefore,

$$SS^{\dagger}_{mm} = \sum_{m'} \mid \hat{r}_{m'm} \mid^2 + \sum_{l} \mid \hat{t}_{lm} \mid^2 = \mathbb{1}. \tag{1.36}$$

Here, t_{lm} is the transmission amplitude of the electron coming from the left channel to the right. On the other hand, $r_{m'm}$ indicates the reflection amplitude of the electron coming from the left channel m to the left channel m'. The electron coming from the left in channel m can be transmitted to the right or reflected. However, the total probability is always conserved (Nazarov and Blanter, 2009).

1.5. Transmission Eigenvalues

Transmission eigenvalues give information about the transport process. They can obtained from the eigenvalues of the transmission product matrix $\hat{t}\hat{t}^{\dagger}$. Therefore, they are also directly related to the scattering matrix mentioned in the previous section. Since the scattering matrix is unitary, the eigenvalues are real numbers. Depending on the disorder configuration of the system, the transmission eigenvalues can take different values. For sufficiently large ensembles, these possibilities indicate a distribution.

The magnitudes of these eigenvalues can be used to determine the open channels in the system. Their magnitudes can change between 0 and 1. They indicate the closed and open channels, respectively.

In general form, the transmission distribution mathematically can be represented as

$$P(T) = \langle \sum_{N} \delta(T - \mathcal{T}_N(E)) \rangle. \tag{1.37}$$

Here, $\mathcal{T}_N$ indicates transmission eigenvalues whose magnitude changes depending on the disorder configuration.

In the eigenchannel basis, there is no interaction between the transport channels. As a result of that, the transmission and the reflection matrices are diagonal, including $\hat{t}\hat{t}^\dagger$ matrix. Because of the diagonality, the transmission eigenvalues and the transmission coefficients of the channels refer to the same parameter. Therefore, in this case, it is possible to think of the system as a parallel circuit with independent transmission channels (Nazarov and Blanter, 2009).

The Landauer Formula can also be written in terms of the transmission eigenvalues at zero temperature as

$$G = G_0 \sum_{n=1}^{N} \mathcal{T}_N \tag{1.38}$$

where $G_0 = 2e^2/h$ and indicates the conductance quantum with a spin factor 2 (Fisher and Lee, 1981). Another definition of the conductance is the ratio of the average current $\bar{I}$ to the voltage difference V, in the case of a small voltage limit. The average current, on the other hand, is time-dependent and can be written as

$$I(t) = \bar{I} + \delta I(t). \tag{1.39}$$

The fluctuations can be described as moving away from the actual value and having a particular name: shot noise (Beenakker, 1997).

1.5.1. Quantum Shot Noise

The quantum shot noise appears as a time-dependent fluctuation in the current via temporal correlations. Their origin is based on the discrete nature of the electron charge. These fluctuations provide information on transport that can not obtained from conductance. The averaged current term, from the Landauer formula, can be written as

$$\bar{I} = \frac{2e^2}{\hbar} V \sum_{n=1}^{N} \mathcal{T}_N \tag{1.40}$$

where V is the applied voltage, $\mathcal{T}_N$ is the transmission eigenvalues, $e^2/\hbar$ is the conductance quantum and 2 comes from the spin factor (Büttiker, 1990).

Schottky realized the first observations of shot noise on vacuum tubes (Schottky, 2018). In a vacuum tube, electrons are emitted by the cathode randomly. Schottky discovered that during this process, in addition to thermal noise, there is another noise resulting from the discreteness of the electrical charge called shot noise. The shot noise, at zero temperature, can be written in terms of the transmission eigenvalues as

$$S = \sum_{n=1}^{N} \mathcal{T}_N(1 - \mathcal{T}_N) \tag{1.41}$$

Here, the terms $\mathcal{T}_\mathcal{N}$ and $1 - \mathcal{T}_N$ indicates the transmission and the reflection probabilities respectively (Büttiker, 1990). From equation 1.41, it can be seen that the Shot noise can not be obtained directly from the transmission probabilities. First, the transmission and reflection probabilities must be multiplied for each eigenchannel; then, their sum should be taken. Since this is the basis-dependent definition, the possibility of the interference of the channels should considered.

During the shot noise calculations, the Pauli principle also becomes essential. The term, $1-\mathcal{T}_N$, in the equation, is responsible for noise reduction and comes from the result of the exclusion principle. This term represents the correlations between the electrons (Blanter and Büttiker, 2000).

If we examined this equation considering the case of the channels open or closed, if the channels completely open $\mathcal{T}_N = 1$ or closed $T_N = 0$ do not contribute to the shot noise. To obtain the maximum contribution, T_N must be 0.5. In the limit of $\mathcal{T}_N \ll 1$ case, the shot noise becomes Poisson noise, which is discussed by Schottky before.

$$S_P = \sum_{1}^{N} \mathcal{T}_N = 2e\langle \bar{I} \rangle \tag{1.42}$$

1.5.2. Fano Factor

The most general definition of the Fano factor is the ratio of the variance to the mean. This definition is mainly used in statistics. While mentioning the transport calculations, on the other hand, the definition becomes more specific and determined as this ratio of the shot noise to the average current. This definition is

the particular type of general one that focuses on current fluctuations. Since it is a universal parameter, the magnitude of the Fano factor is independent of the sample size or band structure. This property makes the Fano factor a crucial indicator for understanding a material's transport properties. The Fano factor can be calculated in terms of the transmission eigenvalues as (Blanter and Büttiker, 2000)

$$F = \frac{\sum_{n=1}^{N} \mathcal{T}_N(1-\mathcal{T}_N)}{\sum_{n=1}^{N} \mathcal{T}_N} \tag{1.43}$$

In the Poisson limit, the transmission eigenvalues are much smaller than one, which indicates pure tunneling. Since $\mathcal{T}_N \ll 1$, the term will be $(1-\mathcal{T}_N) \approx 1$. As a result, the Fano factor also becomes 1. This limit is called an uncorrelated stochastic process. In that case, without taking the limit, the magnitude of the Fano factor can be guessed. Since the distribution is Poissonian, the variance and the means of the distribution give the same value. Therefore, from the general definition of the Fano factor, indicated in equation 1.43, this ratio becomes 1.

For the ballistic conductors, since $\mathcal{T}_N \approx 1$ and $(1-\mathcal{T}_N) \approx 0$, the Fano factor becomes 0. For the other cases, eigenvalue distributions must be used to calculate the Fano factor. For instance, the eigenvalue distributions are bimodal for diffusive wire with a density and can be written as

$$\rho(T) \approx \frac{1}{T\sqrt{(1-T)}}. \tag{1.44}$$

Moreover, according to the linear statistics (in a small voltage limit) eigenvalues can be calculated in the Fermi surface and discrete sum can be converted to integral as

$$\left\langle \sum_{n=1}^{N} \mathcal{T}_N(1-\mathcal{T}_N) \right\rangle = \int \rho(T)T(1-T)dT \tag{1.45}$$

When the integral solved by using integration by parts, the Fano factor obtained as 1/3 for diffusive wire. The Fano factor has other universal values, including dirty interface $F = 1/2$ and $F = 1/4$ for the symmetric ballistic chaotic cavity (Blanter and Büttiker, 2000).

CHAPTER 2

METHODOLOGY

2.1. Green's Function Method

Green's functions provide a way to calculate transport quantities related to the system, like the density of states and transmission function, without solving the eigenvalue equation for the whole system. In other words, it is a practical way to solve the Schrödinger equation.
The Green's function can be defined in general form as

$$((E + i\eta) - H)G(E) = 1. \tag{2.1}$$

where η is an infinitesimal positive small number. In the case of the constant perturbation added to system as $|\psi'\rangle$ the response becomes

$$|\psi\rangle = -G(E)\,|\psi'\rangle\,. \tag{2.2}$$

From this equation, it is interpreted that the role of Green's function is describing the response of the system to a constant perturbation (Datta, 1997).

2.1.1. The Tripartite System

In our calculations, we used a tripartite system where the central region is connected to two semi-infinite periodic leads with both ends. Figure 2.1 shows the representation of this system. The total Hamiltonian can be expressed by a block

tridiagonal matrix as

$$H_{tot} = \begin{pmatrix} H_L & H_{LC} & H_{LR} \\ H_{CL} & H_C & H_{CR} \\ H_{RL} & H_{RC} & H_R \end{pmatrix} \tag{2.3}$$

where H_{LL}, H_{RR}, H_{CC} are Hamiltonians of the left lead, right lead, and center, respectively. H_{LC} and H_{CL} are the interaction Hamiltonians between the system and leads. If there is no direct interaction between leads, H_{LR} and H_{RL} are taken as zero.

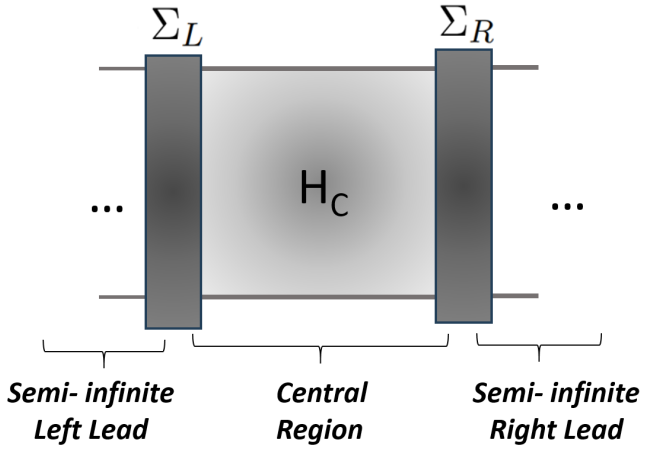

Figure 2.1. Representation of the tripartite system where Σ_L and Σ_R represent the self-energies of the left and right lead, respectively.

For the tripartite system, Equation 2.1 can be written as

$$\begin{pmatrix} E - H_L & -H_{LC} & 0 \\ -H_{CL} & E - H_C & -H_{CR} \\ 0 & -H_{RC} & E - H_R \end{pmatrix} \begin{pmatrix} G_L & G_{LC} & G_{LR} \\ G_{CL} & G_C & G_{CR} \\ G_{RL} & G_{RC} & G_R \end{pmatrix} = \begin{pmatrix} 1 & 0 & 0 \\ 0 & 1 & 0 \\ 0 & 0 & 1 \end{pmatrix} \tag{2.4}$$

By solving this equation for the second column of the Green's function of the central region is obtained as

$$G_C = ((E + i\eta^+)I - H_C - \Sigma_L - \Sigma_R))^{-1}. \tag{2.5}$$

Here, Σ defines the self-energies for the left lead $\sum_L = H_{CL} g_L H_{LC}$ and the right lead $\sum_R = H_{CR} g_L H_{RC}$. Self-energy represents the contribution of the lead effects on the system. g_R and g_L, on the other hand, are surface green functions. Thanks to the periodic structure of the reservoirs g_R and g_L can be calculated by using some decimation techniques.

Since the system is tripartite, the total wave function consists of three subspaces, which are $|\psi_L\rangle, |\psi_R\rangle$ are the wavefunctions for the left and right lead, and $|\psi_C\rangle$ for the central system. Considering the first lead as isolated from the central region and the second lead, the wavefunction on the total system resulting from the incoming wave in the left lead can be calculated. In this case, the coupling between the device and leads can be thinking as a perturbation. The wavefunction $|\psi_L\rangle$ consists of two terms. $\left|\psi^0_{L,n}\right\rangle$ represents the eigenstates of the H_L, $|\psi^{rsp}_L\rangle$ on the other hand, is the response of the total system.

From the solution of the Schrödinger equation for the wavefunction ($\left|\psi^0_{L,n}\right\rangle + |\psi^{rsp}_L\rangle$).

$$E\left|\psi^0_{L,n}\right\rangle + H_{CL}\left|\psi^0_{L,n}\right\rangle + H\left|\psi^{rsp}_L\right\rangle = E\left|\psi^0_{L,n}\right\rangle + E\left|\psi^{rsp}_L\right\rangle \tag{2.6}$$

Therefore,

$$(E - H)\left|\psi^{rsp}_L\right\rangle = H_{CL}\left|\psi^0_{L,n}\right\rangle \tag{2.7}$$

and the response of the total system when the perturbation is $(-H_{CL}|\psi_{1,n}\rangle)$ obtained as

$$|\psi^{rsp}_L\rangle = G H_{CL}\left|\psi^0_{L,n}\right\rangle \tag{2.8}$$

The wavefunction for the left lead becomes

$$|\psi_L\rangle = \left|\psi^0_{L,n}\right\rangle + G_{LC} H_{CL}\left|\psi^0_{L,n}\right\rangle \tag{2.9}$$

By using $G_{LC} = g_L H_{LC} G_C$, equation can be written as

$$|\psi_L\rangle = (1 + g_L H_{LC} G_C H_{CL})\left|\psi^0_{L,n}\right\rangle \tag{2.10}$$

The wavefunction for the right lead and the central region can also be obtained in a similar way as

$$|\psi_R\rangle = g_R H_{RC} G_C H_{CL} \left|\psi^0_{L,n}\right\rangle \qquad \text{and} \qquad |\psi_C\rangle = G_C H_{CL} \left|\psi^0_{L,n}\right\rangle \tag{2.11}$$

Since the wave functions written in term of the same eigenstate $\left|\psi^0_{L,n}\right\rangle$, the partial current can be calculated from

$$j = j_L = -j_R = \frac{-ie}{\hbar}(\langle\psi_R| H_{RC} |\psi_C\rangle - \langle\psi_C| H_{CR} |\psi_R\rangle) \tag{2.12}$$

By using equations in 2.11, the partial current becomes

$$j = \frac{-ie}{\hbar} \left\langle\psi^0_{L,n}\right| H_{LC} G^\dagger_C H_{CR} (g^\dagger_R - g_R) H_{RC} G_C H_{CL} \left|\psi^0_{L,n}\right\rangle \tag{2.13}$$

Using the self-energy terms and broadening matrices can simplify this equation. The physical meaning of self-energy is that it represents the contribution of the leads to the system Hamiltonian. They can be written as $\Sigma_R = H_{CR} g_R H_{RC}$ and $\Sigma_L = H_{CL} g_L H_{LC}$ for right and the left lead respectively. Γ, also called the broadening matrix, on the other hand, is defined as $i(\Sigma - \Sigma^\dagger)$. These terms are related to each other. The imaginary part of the self-energies is responsible for the level broadening. As a result, the total current can be rewritten as

$$I = \sum j = \frac{-ie}{\hbar}(\left\langle\psi^0_{L,n}\right| H_{LC} G^\dagger_C \Gamma_R G_C H_{CL} \left|\psi^0_{L,n}\right\rangle) f_L(E') \tag{2.14}$$

where $f_L(E)$ indicates the distribution function of the left lead.
From the Landauer equation we also know that

$$I = \frac{e}{\hbar} \int_{-\infty}^{\infty} dE T(E) f_L(E) \tag{2.15}$$

Therefore, by comparing these two equations, transmission functions can be obtained in terms of the broadening matrices and the central region as (Datta, 1997)

$$T(E) = 2\pi \sum (H_{LC} G_C^{\dagger} \Gamma_R G_C H_{CL}) \delta(E - E') \tag{2.16}$$

$$T(E) = tr(\Gamma_L G_C^{\dagger} \Gamma_R G_C) \tag{2.17}$$

This equation is also called the Caroli formula. In our calculations, we used the Caroli expression to calculate the transmission of the central region.

2.2. Mode-Matching Method

The mode-matching method provides a way to calculate the transmission for individual modes. Because of that, it is essential, especially when working on multi-channel systems.

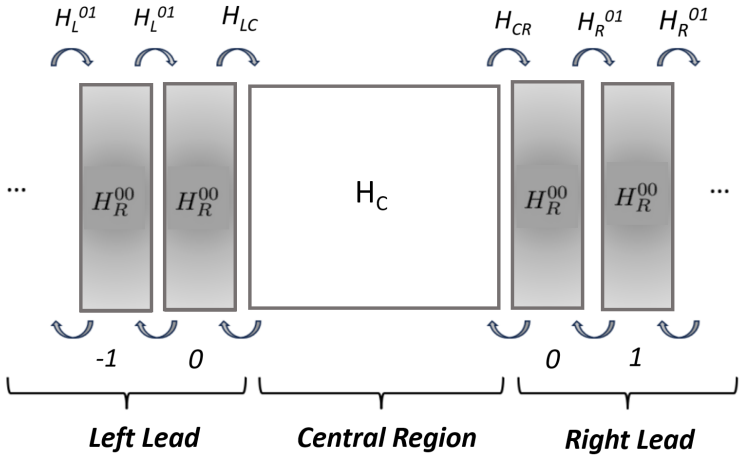

Figure 2.2. The representation of the mode-matching method. Figure is adapted from (Ong and Zhang, 2015)

.

According to this method, the system consists of three parts, as shown in Figure 2.2. Here, since leads are identical and periodic, it is possible to think of them as repeating slices and using the Bloch symmetry. The terms H_L^{01} and H_R^{01} represent

the matrices that provide a coupling between each slice and its neighbor slice on its right side. The indexes L and R indicate the left and right leads, respectively. Bloch matrices are represented with $P_L(-)$ and $P_R(+)$. The + and − signs show left-going and right-going modes. By using the coupling matrices and the surface Green functions (g_L and g_R), the Bloch matrices can be calculated as

$$P_R(+) = g_R H_R^{10} \tag{2.18}$$

$$P_L(-)^{-1} = [H_L^{10} g_L]^{\dagger}. \tag{2.19}$$

After calculating the Bloch matrices, by using the eigenvalue equation, the eigenmodes can be obtained as

$$P_R(+)U_R(+) = \lambda_R(+)U_R(+) \tag{2.20}$$

$$P_L(-)^{-1}U_L(-) = \lambda_L(-)^{-1}U_L(-). \tag{2.21}$$

where $U_R(+)$ and $U_L(-)$ are normalized eigenstates, $\lambda_R(+)$ and $\lambda_L(-)$ eigenvalues of Bloch matrices. If the number of modes represented with m and n in the right and left lead, respectively, from the equation

$$[\lambda_L]_{nn} = e^{ik_n a} \tag{2.22}$$

$$[\lambda_R]_{mm} = e^{ik_m a} \tag{2.23}$$

wave vectors can be calculated in terms of the eigenvalues as

$$k_n = \arccos(\ Re(\lambda_L)) \tag{2.24}$$

$$k_m = \arccos(\ Re(\lambda_R)). \tag{2.25}$$

The k range in the equation is determined as $\hat{a}\pi < k < \pi$. Then, by using eigenvectors of the Bloch matrices, group velocities calculated from

$$Vg_R(+) = U_R(+)^\dagger \Gamma_R U_R(+) \tag{2.26}$$

$$Vg_L(+) = U_L(-)^\dagger \Gamma_L U_L(-). \tag{2.27}$$

Finally, the transmission matrix from the left to the right lead obtained as (Khomyakov et al., 2005; Ong and Zhang, 2015)

$$t_{n,m} = t_{L,R} = i\sqrt{Vg_L(+)}U_L^{-1}(+)G_{LR}U_R^{-1}(-)^\dagger\sqrt{Vg_R(+)} \tag{2.28}$$

where $G_{LR} = g_L H_{LC} G_C H_{CR} g_R$. Since G_{LR} includes the information about the central region, it is possible to see the effects of the defects on the transmission in the system. The transmission matrix product ($t_{nm}t_{nm}^\dagger$), which is equivalent to $|t_{n,m}|^2$, represents the transmission probability from n th mode in the left lead to the m th mode in the right lead. Therefore, the transmission of the nth left lead mode can be calculated from the nth dioganal element of $tt^\dagger$ and can be written as

$$T_n^L = [tt^\dagger]_{nn} \tag{2.29}$$

The transmission of the mth right lead mode, on the other hand, can be calculated from

$$T_m^R = [t^\dagger t]_{mm} \tag{2.30}$$

Therefore, the total transmissions for the left and the right lead becomes

$$T^L = \sum_{n=1}^{N_L} T_n^L = tr(tt^\dagger) \tag{2.31}$$

$$T^R = \sum_{m=1}^{N_R} T_m^R = tr(t^\dagger t) \tag{2.32}$$

Here, N_L and N_R indicates the total number of modes for each channels for left and right lead respectively. The transmission of the left and right leads is equal to each other and also equal to the total transmission obtained in Equation 2.17 (Ong and Zhang, 2015; Khomyakov et al., 2005).

$$T^L = T^R = T \tag{2.33}$$

2.3. Decimation Techniques

Decimation techniques are mainly used to gain speed and memory during calculation. The origin of this technique is based on thinking of matrices as a number of slices. Doing that provides a way of working on large systems efficiently. In our calculations, we used this technique to calculate the surface Green's functions and study the localization regime at a large scale.

The common point of these two calculations is based on the fundamental equation of decimation. The fundamental equation provides a way to write the matrix elements in terms of each other and reduce the dimension of the matrix. At the end of that, we can reach the effective Hamiltonian.

The decimation equation in general form can be obtained by multiplying any matrix with its inverse. For example, if M is any invertible matrix and N is its inverse matrix, their product must be one. In the matrix form, this equation can be written as

$$\begin{pmatrix} M_{11} & M_{12} \\ M_{21} & M_{22} \end{pmatrix} \begin{pmatrix} N_{11} & N_{12} \\ N_{21} & N_{22} \end{pmatrix} = \begin{pmatrix} \mathbb{1} & 0 \\ 0 & \mathbb{1} \end{pmatrix} \tag{2.34}$$

From the matrix equation, we can obtain that

$$M_{21}N_{11} + M_{22}N_{21} = 0. \tag{2.35}$$

Therefore,

$$N_{21} = -M_{22}^{-1}M_{21}N_{11}. \tag{2.36}$$

Substituting this equation into

$$M_{11}N_{11} + M_{12}N_{21} = \mathbb{1} \tag{2.37}$$

gives the fundamental equation of decimation

$$N_{11} = (M_{11} - M_{12}M_{22}^{-1}M_{21})^{-1}. \tag{2.38}$$

This equation also can be used for Green functions. The Hamiltonian matrix for the bipartite system can be written as

$$H = \begin{pmatrix} H_{11} & H_{12} \\ H_{21} & H_{22} \end{pmatrix} \tag{2.39}$$

Then, calculating the inversion of this matrix the Green's function obtained as

$$((E + i\eta)\mathbb{1} - H)^{-1} = G = \begin{pmatrix} G_{11} & G_{12} \\ G_{21} & G_{22} \end{pmatrix} \tag{2.40}$$

From the fundamental equation of decimation

$$G_{11} = ((E + i\eta)\mathbb{1} - H_{11}) - (-H_{12})((E + i\eta)\mathbb{1} - H_{22})^{-1}(-H_{21}))^{-1} \tag{2.41}$$

where $((E + i\eta)\mathbb{1} - H_{22})^{-1} = G_{22}^{0}$. Therefore, the effective Hamiltonian for H_{11} becomes

$$H_{11}^{eff} = H_{11} + H_{12}G_{22}^{0}H_{21} \tag{2.42}$$

The second term $H_{12}G_{22}^{0}H_{21}$ on the right side of the Equation 2.42 indicates the self-energy of System 2 (Nemec, 2007).

At large systems, we performed calculations using an iterative method. This method provides an efficient solution to gain speed and memory during the calculations, especially in the localization regime. The logic behind this method is similar

to the decimation techniques mentioned above for the bipartite systems. The iterative method can be examined in two parts. First, we determined the length of the system and constructed a random defect array at that range for the localization regime. Then, we constructed the $3M \times 3M$ Hamiltonian, where M indicates the number of modes for the system. After that, we decimated the elements of the second layer from the Hamiltonian matrix.

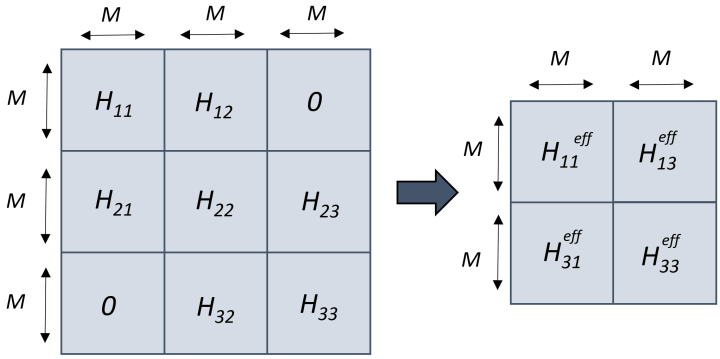

Figure 2.3. An illustration of the change in the dimensions of the Hamiltonian matrix before and after the first decimation.

Figure 2.3 illustrates this step. In this way, the information of the second layer is transferred to the other elements of the matrix. A new matrix, the effective Hamiltonian matrix, was obtained with a dimension of $2M \times 2M$ (Nemec, 2007). This part is nearly the same as the bipartite system mentioned above; the only difference is that the system is tripartite in this case.

After obtaining the effective Hamiltonian once, we determined the iteration amount, which indicates the number of layers added at each iteration. By doing that, we calculated the transmission properties of the system without constructing a complete Hamiltonian. Figure 2.4 is an example of the iteration amount chosen as 2 layers indicated with green blocks. In our calculations for the localization regime, we took the adding number of layer as 100 for each iteration.

Figure 2.5 shows the average transmission energy plot for zigzag graphene nanoribbons. Here, we used one disorder configuration to see the consistency. From the figure, we can see that the same results can be obtained in a short time by using the decimation method.

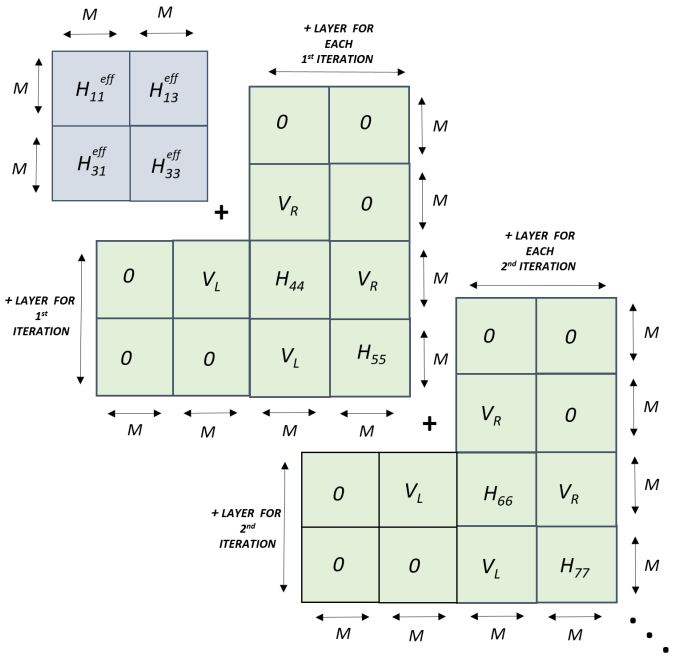

Figure 2.4. An illustration of the iteration process where the number of adding layers is chosen as two for each iteration

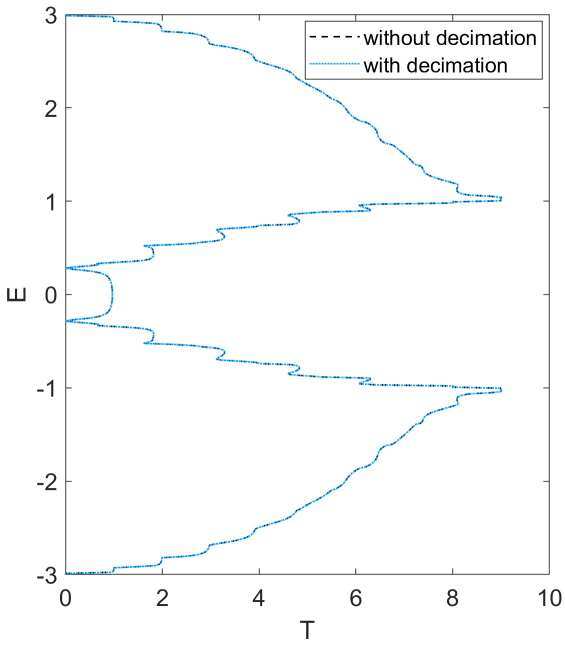

Figure 2.5. The average transmission energy plot for 12-zGNR in the presence of edge disorder

2.3.1. Calculation of the Surface Green's Functions

The surface Green functions play an essential role in calculating self energies, in other words, to calculate the contribution of the leads to the system. In our systems, the leads are semi-infinite. Working with semi-infinite matrices is a problem when taking the matrix inversion. Therefore, to avoid that, we used the renormalization decimation algorithm during the calculations of the surface Green functions.

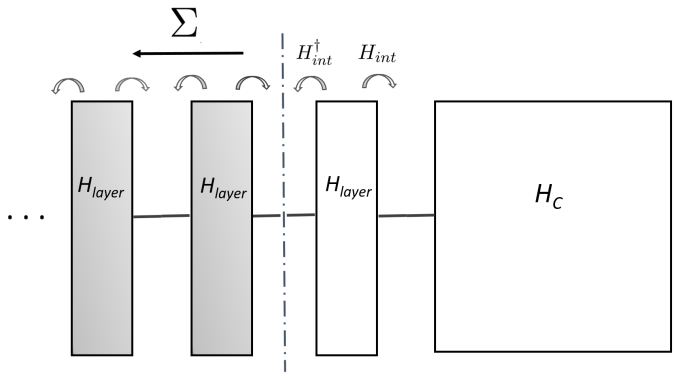

Figure 2.6. The representation of the renormalization decimation method where H_{layer} and H_C indicate the Hamiltonian of each layer and the central region. The term H_int is the interaction Hamiltonian of each layer and its neighbor layer. The self energies of the system are represented with Σ.

As a first step, we defined the Hamiltonian of the leads. They are block tridiagonal and can be written in general form as

$$H_{right} = \begin{pmatrix} H_{00} & H_{01} & 0 & \dots \\ H_{10} & H_{11} & H_{12} & 0 \\ 0 & H_{21} & \ddots & H_{23} \\ \vdots & & & \end{pmatrix} \quad \text{or} \quad H_{left} = \begin{pmatrix} & & & \vdots \\ H_{23} & \ddots & H_{21} & 0 \\ 0 & H_{12} & H_{11} & H_{10} \\ \dots & 0 & H_{01} & H_{00} \end{pmatrix} \tag{2.43}$$

Then, to perform the decimation method, we consider a system as a series of periodic layers. Since each layer is identical, two Hamiltonian is enough to construct the

whole system. We defined these Hamiltonians as H_{layer} and H_{int} briefly. According to this definition, H_{layer} represents the Hamiltonian of each layer while H_{int} is the interaction Hamiltonian for each layer and its neighbor layer. Therefore,

$$\begin{aligned} H_{00} = H_{11} = H_{22} = \cdots = H_{layer} \\ H_{01} = H_{12} = H_{23} = \cdots = H_{int} \end{aligned} \tag{2.44}$$

First, we can think that there are N identical layers, and the last one belongs to the central region, as shown in Figure 2.6. In that case, the rest of the $N-1$ layers belong to the leads. Their contribution to the central region, their self-energies, in other words, can be calculated as

$$\begin{aligned} \Sigma_L = H_{int}^{\dagger} g_{N-1}^{L} H_{int}, \\ \Sigma_R = H_{int} g_{N-1}^{R} H_{int}^{\dagger}. \end{aligned} \tag{2.45}$$

where g_{N-1}^{L} and g_{N-1}^{R} indicate the surface Green functions consisting of $N-1$ slices. Therefore, for N slices case, the surface Green functions for the left lead becomes

$$\begin{aligned} g_N^L = (E + i\eta - H_{layer} - \Sigma_L)^{-1} \\ g_N^L = (E + i\eta - H_{layer} - H_{int}^{\dagger} g_{N-1} H_{int})^{-1} \end{aligned} \tag{2.46}$$

and for the right lead in a similar way

$$\begin{aligned} g_N^R = (E + i\eta - H_{layer} - \Sigma_R)^{-1} \\ g_N^R = (E + i\eta - H_{layer} - H_{int} g_{N-1} H_{int}^{\dagger})^{-1} \end{aligned} \tag{2.47}$$

This equation shows a relation between the case of the N and $N-1$ layers, indicating recursion (Sancho et al., 1985). Since the layers are periodic, the equation can easily be applied to our systems. After a specific iteration, g_N and g_{N-1} converged to the same value, and we can reach the surface green function for our calculations.

CHAPTER 3

MULTI-CHANNEL SYSTEMS

3.1. Two-Channel Model

The two-channel model is a crucial toy model for understanding the link between multichannel systems and anomalous transport behavior. It provides a way to obtain different diffusion mechanisms with the same model by changing system parameters. Because of that, we first studied this model before investigating the transport properties of nanoribbons.

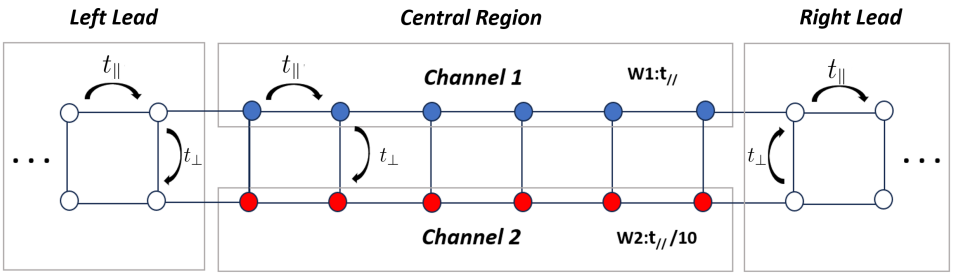

Figure 3.1. The two-channel model with an Anderson disorder strengths $W_1 = t_{\parallel}$ and $W_2 = t_{\parallel}/10$. $t_{\perp}$ and $t_{\parallel}$ indicate the hopping strength between the channels and through the channels respectively.

Figure 3.1 represents the illustration of our two-channel toy model. This model comprises two channels connected with a hopping strength $t_{\perp}$. The ratio between the $t_{\perp}$ and the hopping strength through the channels,$t_{\parallel}$, is a crucial parameter affecting the diffusion type of the system. After constructing a structure, we introduced the Anderson disorder to Channel 1 and Channel 2, whose disorder strengths are represented with W_1 and W_2, respectively. Depending on these values, disorders are generated as random numbers between $-W_{1,2}/2$ and $+W_{1,2}/2$, whose sum equals zero. Since the differences in these disorder strengths affect the group velocities of

channels, by doing that, we aim to work on two channels with different transport properties simultaneously. Finally, we connected this region with two perfect semi-infinite chains from the left and right and calculated the transmission using Green's function method.

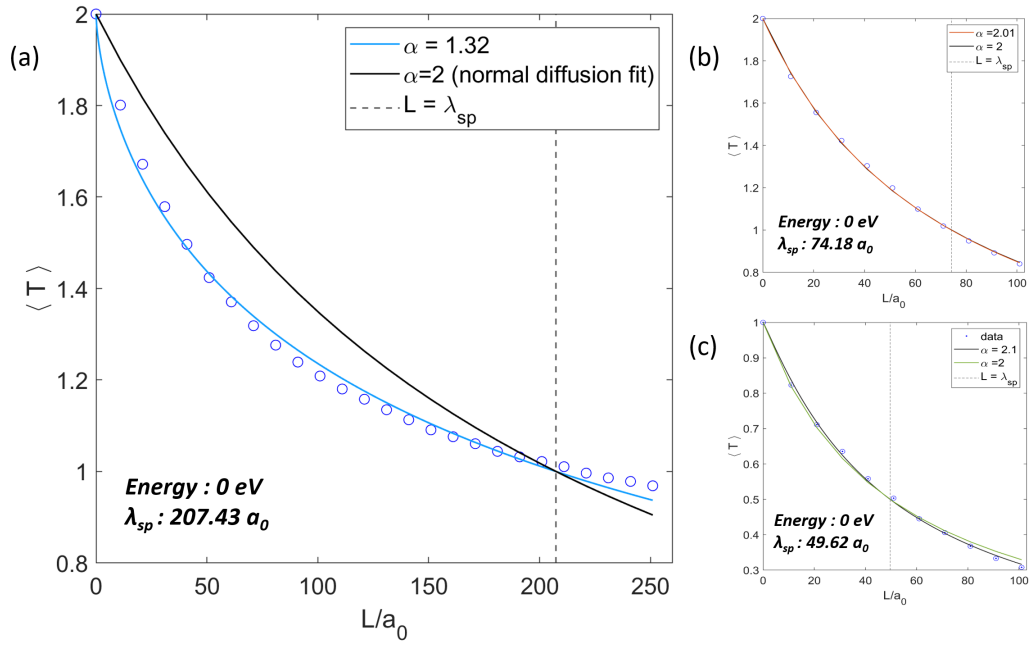

Figure 3.2. The average transmission-length relation over 1000 different disorder configurations for (a) the two-channel model with $W_1 = t_\parallel, W_2 = t_\parallel/10, t_\perp/t_\parallel = 1/20$, (b) the two-channel model with $W_1 = t_\parallel, W_2 = t_\parallel/10, t_\perp/t_\parallel = 1$ and (c) the single-channel model with $W = t_\parallel$, at the 0 eV.

Figure 3.2 shows the relation between the average transmission and the system length calculated from the Green's function method over 1000 different disorder configurations. The results in Figure 3.2.a and 3.2.b belong to the two-channel model with Anderson disorder strengths $W_1 = t_\parallel$ and $W_2 = t_\parallel/10$. The main difference between these two structures is the $t_\perp/t_\parallel$ ratio. In Figure 3.2.a $t_\perp/t_\parallel$ ratio is taken as $1/20$ and in Figure 3.2.b as 1. Figure 3.2.c, on the other hand, shows the results for a single-channel model with an Anderson disorder $W = t_\parallel$. According to the results, the average transmission decreases with system length in the presence of disorder.

The curves in the figures, represented by blue, red, and green colors, are obtained using a generalized diffusion equation indicated in Equation 1.16. α and λ_{sp} were chosen as free parameters during the fitting process. The black curves, on the other hand, are obtained from the transmission formula indicated in Equation 1.13. This equation is the particular type of the generalized transmission formula, where α equals two. According to our results, these curves coincide in Figures 3.2.b (single-channel model) and 3.2.c (two-channel model with $t_\perp/t_\parallel = 1$). This behavior confirms that α values are 2 for these systems and shows normal diffusion. However, in Figure 3.2.a, α was obtained as 1.32, and the system shows anomalous diffusion. Furthermore, from the fitting, we obtained the spread length, λ_{sp}, for these systems which are $207.43a_0$, $74.18a_0$ and $49.62a_0$ for the two-channel model with $t_\perp/t_\parallel = 1/20$, $t_\perp/t_\parallel = 1$ and the single-channel model. The spread lengths are indicated with a dashed line. At these lengths, the black curves and the colored fitting curves coincide.

Then, we investigated the change in the resistance with an increasing system length. From the four probe equation,in the normal diffusion regime, we know that resistance is proportional to L/λ_{sp} ratio and can be calculated from

$$R_4 = \frac{1}{M}\frac{L}{\lambda_{sp}}. \tag{3.1}$$

Accordingly, for the generalized case, one can write

$$R_4 = \frac{1}{T} - \frac{1}{M}. \tag{3.2}$$

where M is the number of modes, and T is the transmission.

In our calculations, we used Equation 3.2 for both $t_\perp/t_\parallel = 1$ (normal diffusion) and $t_\perp/t_\parallel = 1/20$ (anomalous diffusion) case to calculate the resistance. From Figure 3.3.a, we can see that, in the normal diffusion case, the resistance increases linearly with system length. However, in the anomalous diffusion case, this behavior becomes sub-linear. In Figure 3.3.b, we multiplied the four-probe resistance with the number of modes M for both cases and investigated the mode-independent case. According to this figure, two curves coincide where the system length becomes equal to the spread length. The differences between the changes in the resistance behavior

can be seen more clearly up to that point. Lastly, in Figure 3.3.c, we investigated the logarithmic scale and focused on the slopes. From the generalized transmission equation in the diffusion regime, we know that the slope of the lines in Figure 3.3.c have slopes $\alpha/2$.

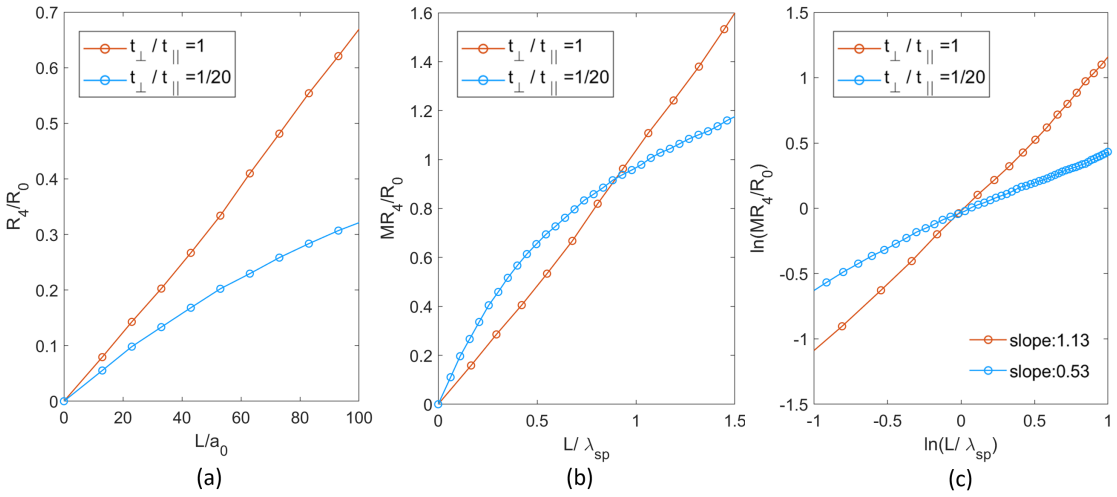

Figure 3.3. The resistance-system length relations of the two-channel model for (a)the mode-dependent version (b)the mode-independent version (c) the logarithmic version.

After determining the characteristic differences between normal and anomalous diffusion, we focused on the possible reasons behind this anomaly. In the literature, anomalous diffusion is mainly observed due to Levy disorder. However, we used Anderson disorder in our calculations, which has a mechanism different from the literature. To understand the reason behind this, we utilized the mode-matching method and investigated the transmissions of the channels individually.

As a reference point, first, we constructed a single channel with the hopping strength $t_{\parallel} = 1$ and the Anderson disorder W $=t_{\parallel}$. By doing that, we aim to see the possible shapes and the average values of the transmission distributions. According to our results in Figure 3.4, three characteristic distribution types exist: nearly ballistic ($L = 23a_0$), diffusion ($L = 43a_0$), and nearly localization ($L = 103a_0$) where the average transmissions are 0.70, 0.55 and 0.30, respectively. The magnitudes of the transmission probabilities can take values between 0 and 1. Therefore, in these figures, the maximum value of the x-axis gives information about the number of open

channels in the system. For the pristine case, the transmission probability takes its maximum value of 1. After a disorder is introduced to the system, the transmission decreases. For large ensemble sizes, the possible transmission probabilities give distributions. While studying with the single channel, it is easier to observe these regimes since the system has one mode. However, the mode analysis becomes more complicated for the two-channel model than for the single-channel case.

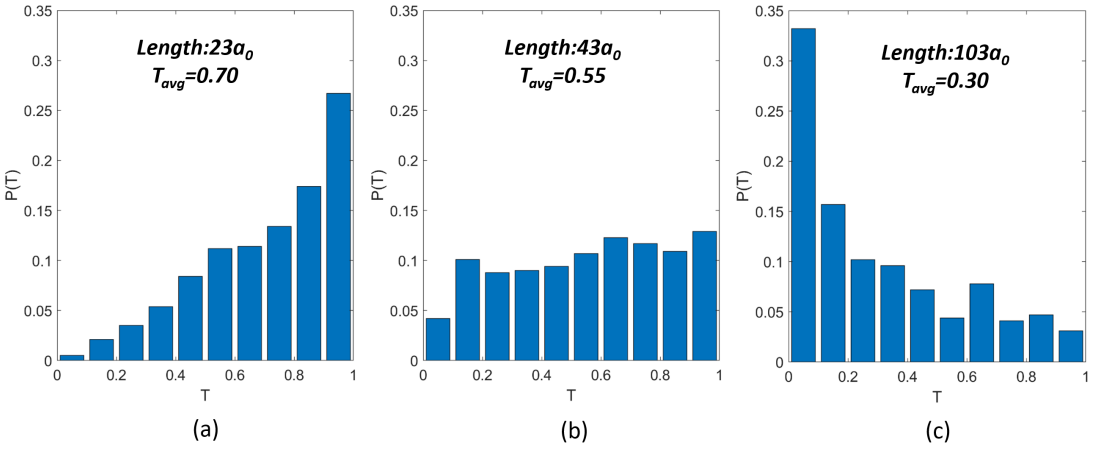

Figure 3.4. The transmission probability distributions for single-channel over 1000 different disorder configurations for $L = 23a_0$, $L = 43a_0$ and $L = 103a_0$.

The transmission distributions obtained for the two-channel model are a combination of the results for the single channel case. Based on the single channel results, there are typically six possible mathematical configurations for two-channel case: ballistic+ballistic, ballistic+diffusion, diffusion+diffusion, diffusion+localization, ballistic+localization, and localization+localization. However, we observed five combinations in the anomalous case, as shown in Figure 3.5. The main reason behind that is that Channel 1 has a stronger disorder than Channel 2 and enters localization faster, which makes the diffusion+diffusion case impossible for systems that show anomalous diffusion.

Figure 3.5 shows the transmission probability distributions for the two-channel model over 1000 different disorder configurations using the mode-matching method and Green's function method. First, we calculated the transmission probabilities of the channels individually, which are indicated as t_1 and t_2 for the Channel 1 and the Channel 2, respectively.

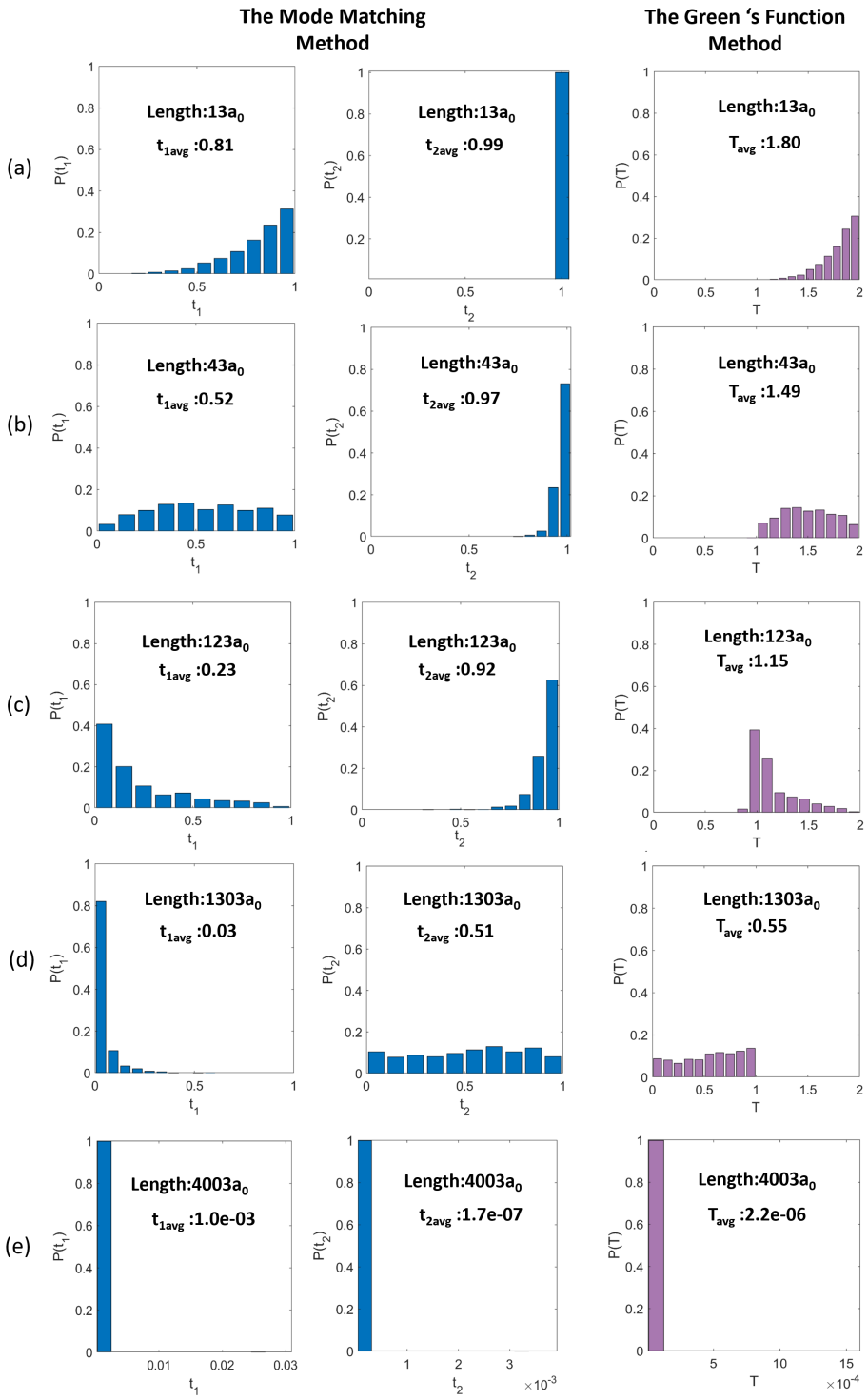

Figure 3.5. The transmission probability distributions at different lengths for (a)$L = 13a_0$ (b)$L = 43a_0$ (c)$L = 123a_0$ (d)$L = 1303a_0$ (e) $L = 4003a_0$ obtained from the mode-matching method for Channel 1 $P(t_1)$ and Channel 2 $P(t_2)$, from the Green's function method for the total system.

In Figure 3.5.a, the system length is taken as $13a_0$. At that length, the average transmission probabilities obtained from the mode-matching method, as $t_{1avg} = 0.81$ and $t_{2avg} = 0.99$, closer to 1. Furthermore, the transmission probability distribution of both channels has similar shapes in Figure 3.4.a, which indicates the ballistic regime. At $L = 43a_0$, shown in Figure 3.5.b, the transmission probability of Channel 1 decreases, and its average becomes 0.52, whose shape and the average are closer to the distribution in Figure 3.4.b, indicating the diffusion regime. At that length, Channel 2 is still in the ballistic regime with an average transmission probability of 0.97. When the system length is $123a_0$, the average transmission probability of Channel 1 becomes 0.23, and the shape of the distribution becomes similar to Figure 3.4.c, which indicates a localization regime. This decrease in the transmission probability of Channel 1 resulted from the strong disorder. In the normal diffusion case, since channels are strongly coupled, instead of this ballistic + localization regime, we can observe diffusion+ diffusion regime. In Figure 3.5.d, the system length is taken as $1303a_0$, and the average probability of Channel 2 becomes 0.51, indicating a diffusion regime. Channel 1, on the other hand, is still found in the localization regime. Lastly, at $4003a_0$, both Channels are found in the localization regime with an average transmission probability as $t_{1avg} = 1.0e-03$ and $t_{2avg} = 1.7e-07$.

After that, we compared these distributions with total transmission distributions T obtained from Green's function method, as indicated in Equation 2.18. This time, since the total number of modes is two, the x-axis range changes between 0 and 2. In this figure, we can see that the summation of the t_1 and t_2 is nearly equal to T, confirming that our calculations using different methods are consistent.

The mode matching method also provides a way to visually see the magnitudes of the transmission probabilities on the bands by using color codes. Since the transmission probability changes between zero and one, we set the color bar by choosing its limits according to these values. Figure 3.6 shows the band resolved probabilities for two-channel model at different system lengths. According to the color codes, red tones indicate high transmission while blue tones indicate low transmission. The black color, indicates the transmission probability closer to zero and shows localization. From the figures, we can see that, when the length increases the colors of the bands changes from red to black. Furthermore, it can be observed that Channel 1 enters localization faster than Channel 2.

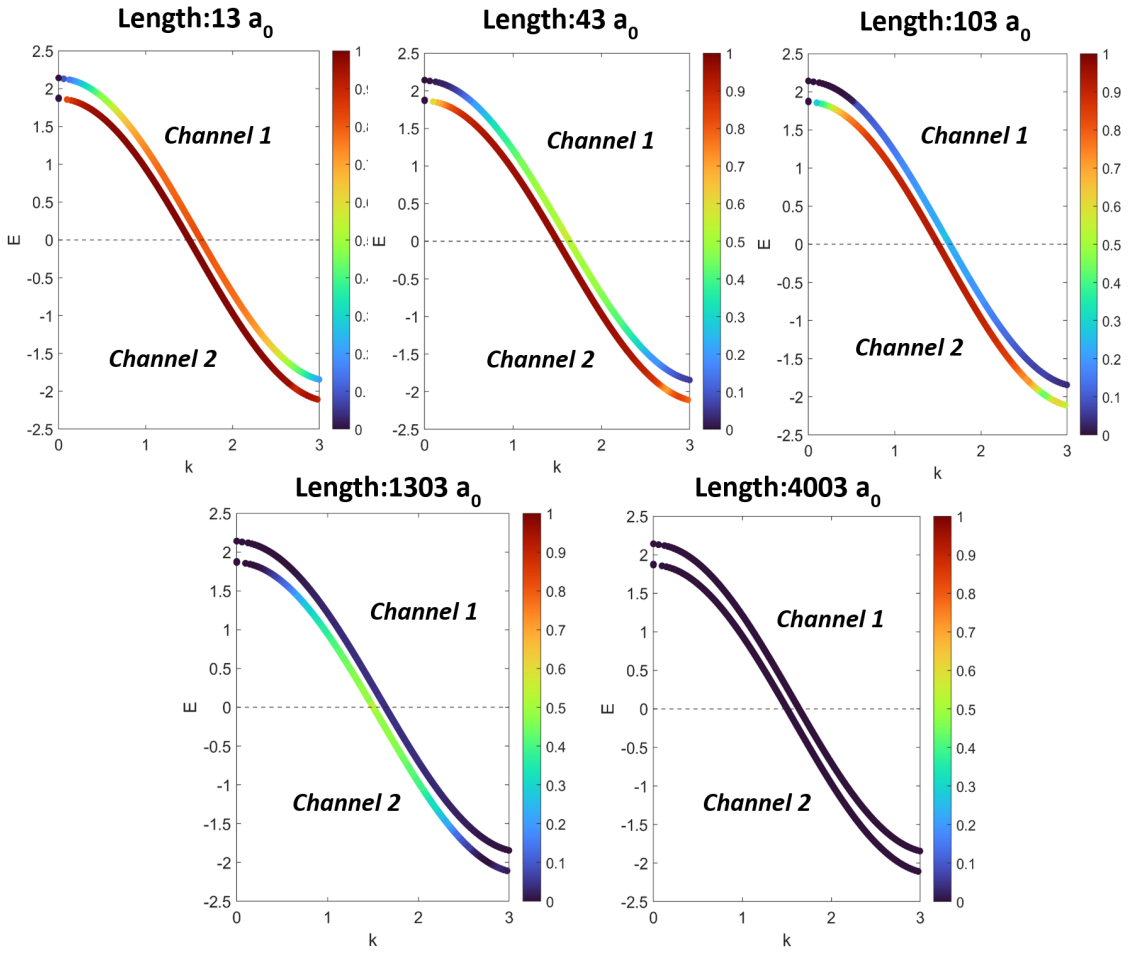

Figure 3.6. The band resolved probabilities for the two-channel model at different system lengths. The color bars show the magnitudes of the transmission probabilities obtained from the mode-matching method.

As a final step, we calculated the Fano factor to understand the effects of the anomaly in physical concepts. To do that, after calculating the transmission matrix t from the mode-matching method, we multiplied it with its Hermitian conjugate $t^{\dagger}$ and obtained the transmission matrix product. Using the eigenvalues of this matrix in equation 1.40, we obtained the Fano factor for different lengths.

Figure 3.7 belongs to a two-channel system where $t_{\perp}/t_{\parallel} = 1/20$ and shows anomalous diffusion. Here, the Fano factor increases with length first, then decreases to nearly $207.43a_0$. This value indicates the spread length of this system. After passing the spread length, it again increases sub-linearly. Our results showed that the Fano factor has turning points in the anomalous diffusion case. On the other

hand, in Figures 3.7.b and 3.7.c, there is no turning point, and the Fano factor increases monotonically with the system length.

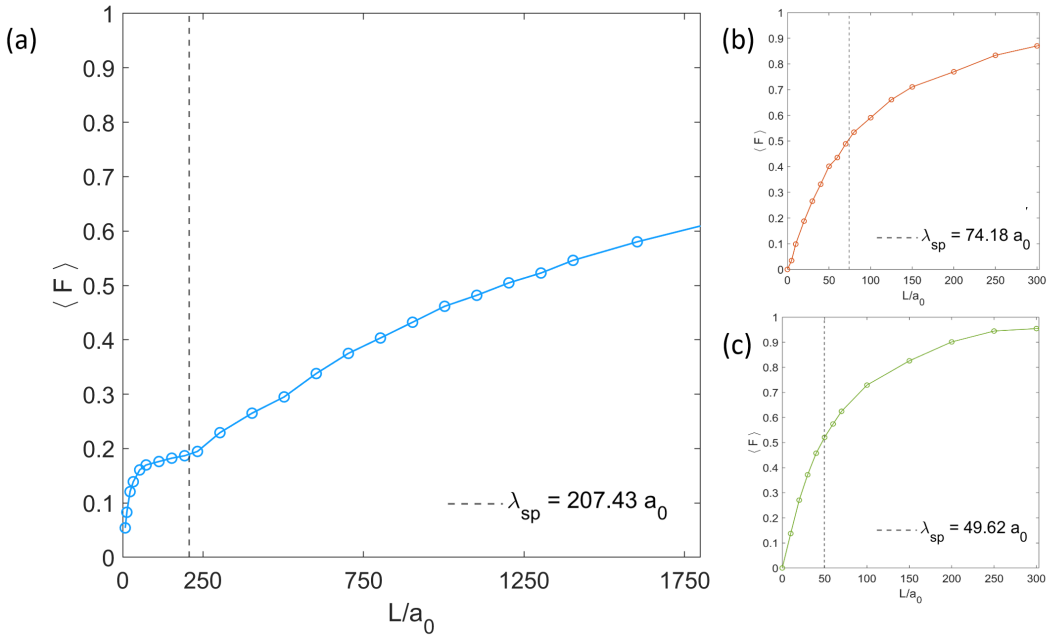

Figure 3.7. The average Fano factor- system length relation for (a) two-channel system with $t_\perp/t_\parallel = 1/20$ (anomalous diffusion) (b) two-channel system with $t_\perp/t_\parallel = 1$ (normal diffusion) (c) single-channel (normal diffusion) at $0eV$. The dashed line indicates the spread length of the systems.

Figure 3.8.a investigates the change in the transmission eigenvalues T_1 and T_2 with system length. This figure shows two different paths. The red path belongs to the normal diffusion case, while the blue one indicates anomalous diffusion. The data points on the lines belong to different system lengths. As a common point, both paths start where the eigenvalues equal nearly one since the systems are initially in a Ballistic regime. After some point, because of the defects in the system, their eigenvalues decrease with length. In the normal diffusion case, since the speed of this change is the same for both channels, we obtained a linear red path. On the other hand, for the anomalous diffusion case, indicated with the blue path, decreasing shows non-linear behavior. T_1 decreases much faster because of the strong disorder

and enters localization while T_2 is nearly equal to 0.7 (quasi-ballistic regime). In other words, two channels can be found in different transport regimes simultaneously.

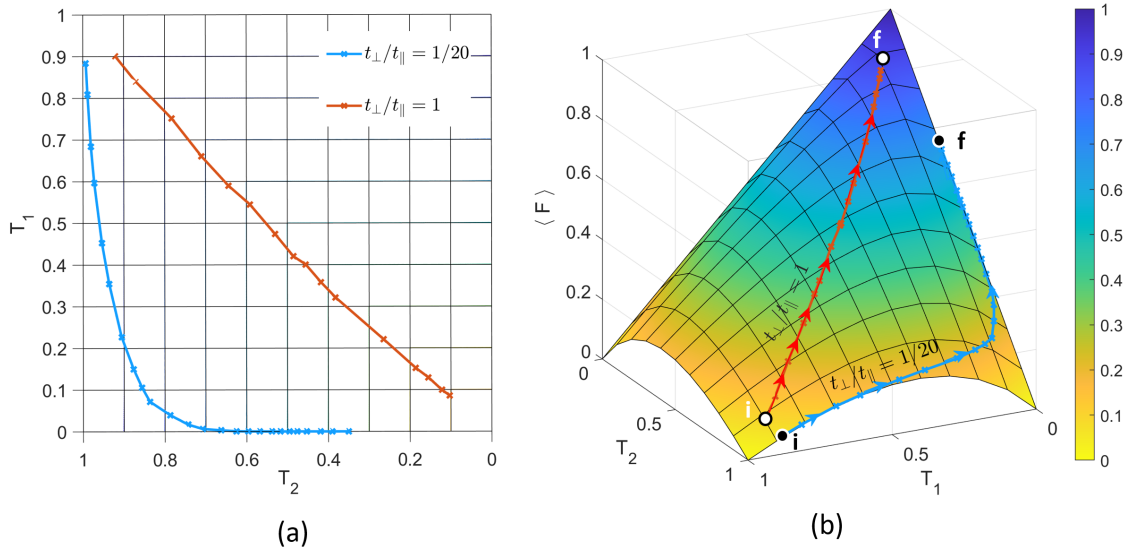

Figure 3.8. (a) The change in the transmission eigenvalues T_1 and T_2 with system length (b) The path of the transmission eigenvalues on the Fano vector space.

In Figure 3.8.b, we determined a surface that shows all possible Fano factor values changing from 0(yellow) to 1(blue). This change depends on the transmission eigenvalues represented with red and blue paths for normal and anomalous diffusion. In the normal diffusion, the change in the Fano factor through the path shows monotonic behavior with an increasing length. The colors change from yellow to blue with an increasing length. In the anomalous diffusion, until T_1 becomes nearly zero and enters localization, the Fano factor is found in the yellow region. After that point, the Fano factor increases faster and reaches the blue area. In other words, if the system has anomalous diffusion, the change in the Fano factor becomes non-monotonic.

3.2. Nanoribbons with a Hexagonal Lattice

In this section, we investigated the transport properties in hexagonal lattices, including graphene and quartic nanoribbons.

Graphene nanoribbons are quasi-one-dimensional honeycomb lattices consisting of carbon atoms. Because of their electronic (Barone et al., 2006), optical (Prezzi et al., 2008), magnetic (Enciu et al., 2014), and thermal properties (Campos-Delgado et al., 2009), they have a wide range of application areas, including nanoelectronic devices.

Quartic materials also have hexagonal structures like graphene nanoribbons, separated by different hopping strength ratios from them. They consist of III (Ga, In)-VI (S, Se), IV (C, Si, Pb, Ge, Sn)- V (N, P, Sb, Bi, As) or group V elements. Their characteristic property is a quartic dispersion at their valance band, which leads to strong scatterings (Sevinçli, 2017; Özdamar et al., 2018; Çınar et al., 2021). Furthermore, they have sharp singularities, van Hove singularities (Van Hove, 1953) in their density of states. Because of their unique properties, including thermoelectric efficiency and magnetic instability, quartic materials are promising candidates for investigation of transmission in nanoscales.

3.2.1. Electronic Structure

In our calculations, we used tight binding Hamiltonian, which includes first and second nearest neighbor interactions and can be written as

$$H = -t_1 \sum_{\langle i,j \rangle} (a_i^\dagger a_j + hc) - t_2 \sum_{\langle\langle i,j \rangle\rangle} (a_i^\dagger a_j + hc). \tag{3.3}$$

Here, $a_i^\dagger$ creates an electron at the ith site while a_j annihilates at the jth site. The terms t_1 and t_2 indicate the first nearest neighbor and the second nearest neighbor interaction terms, respectively. They have a crucial role in shaping the electronic band structure of the materials. In order to see that, the band energies can be calculated from

$$E_{-}^{+}(k) =_{-}^{+} t_1 \sqrt{3 + f(k)} - t_2 f(k) \tag{3.4}$$

where $f(k)$ indicates

$$f(k) = 2\cos\left(\sqrt{3}k_y a\right) + 4\cos\left(\sqrt{3}k_y a/2\right).\cos(3k_x a/2) \tag{3.5}$$

Here, k represents a vector in reciprocal space, and a is the lattice constant. The main difference between the graphene and quartic nanoribbon band structures originates from the t_2/t_1 ratio. If E_+/t_1 ratio is expanded around a Γ point on the reciprocal space, by using Taylor's expansion, it becomes

$$E_+/t_1 \simeq (3 - 6(t_2/t_1)) - (ka)^2(3 - 18(t_2/t_1)/4 + (ka)^4(3 - 54(t_2/t_1)/64). \tag{3.6}$$

This equation has a critical point at Γ when $t_2/t_1 = 1/6$. Because, in the case of $t_2/t_1 = 1/6$, the quadratic term vanishes, and the quartic term becomes dominant. For the cases where $t_2/t_1 > 1/6$, strong singularities occur in the density of states. As a result, Mexican hat-like dispersion is observed in band structures (Sevinçli, 2017). In our models, we took this ratio as 0 for graphene, while 1/5 for quartic nanoribbons.

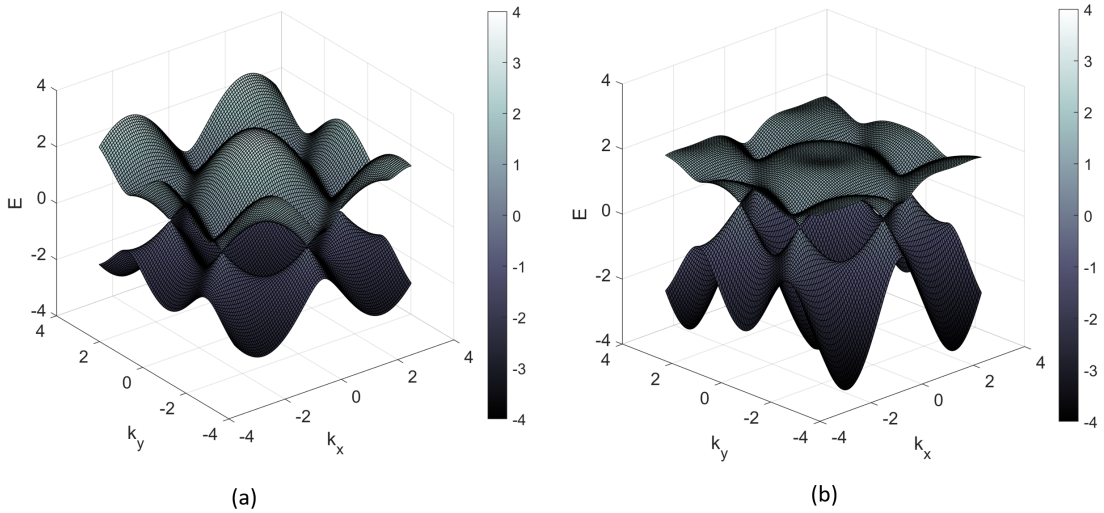

Figure 3.9. The electronic band structure of the (a) graphene ($t_2/t_1 = 0$) (b) quartic materials ($t_2/t_1 = 1/5$), in 3D space.

Figure 3.9 shows the electronic band structure of graphene and quartic materials. Nanoribbons can be obtained by cutting quasi-one-dimensional strips from these sheets. They are suitable candidates to investigate the edge effects of the materials. According to the cutting direction, nanoribbons can have edges whose shapes are zigzag, armchair, or a combination of both (Das and Rahaman, 2017).

3.2.2. The Contribution of Edge and Bulk States

Before studying transmission calculations, we first investigated the edge-bulk state contributions in the energy band diagram. Because, in our models, defects are introduced only to edge atoms, the transmission probabilities will be different at the modes where the effects of the edge atoms are dominant. As a result, the modes of the nanoribbons behaved like channels with different physical properties, similar to the two-channel toy model.

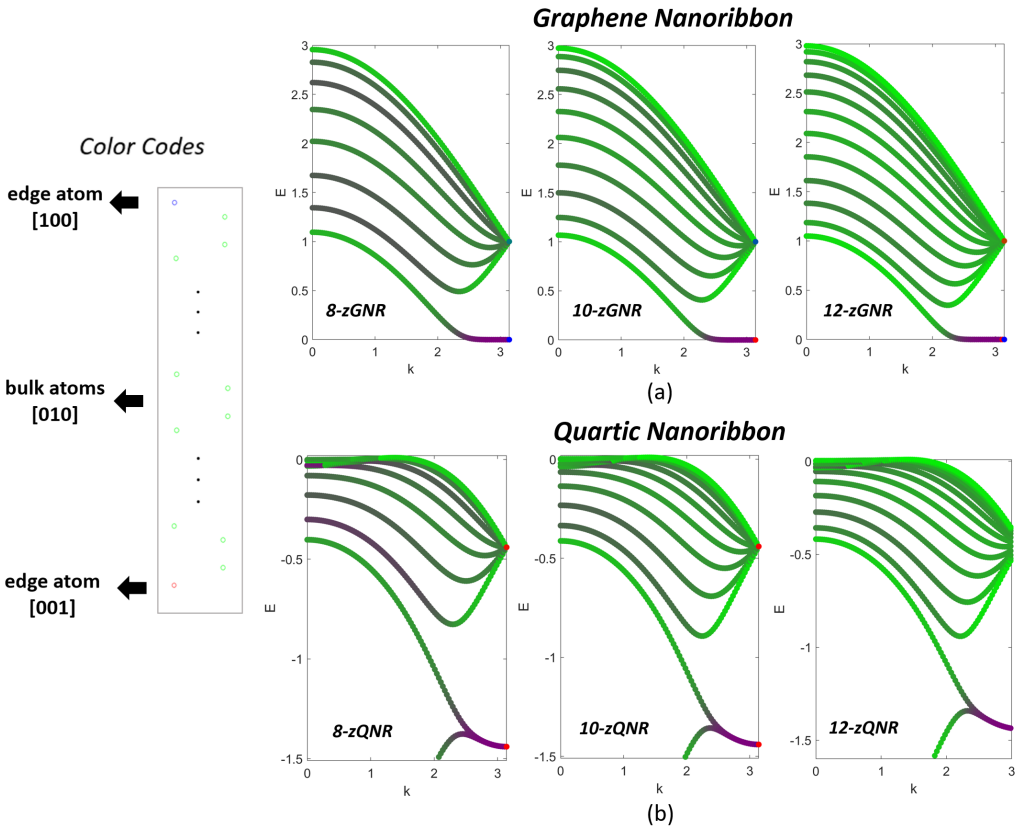

Figure 3.10. The contribution of the edge and bulk states on the energy band diagram is represented with color codes for (a) zGNR (b) zQNR

To analyze the contributions, we constructed a model where the probability density of the eigenvectors is indicated by different colors, considering the position of the atoms. In Figure 3.10, the edge states are indicated by blue and red, while bulk states are indicated by green. This representation shows magenta[101] regions formed on the band diagram, especially for 8zGNR and 8zQNR. These regions resulted from combining blue [001] and red [100] states. In these regions, the effects of the edge atoms are more dominant than bulk atoms. Furthermore, some bands formed as tones of green. Since dark green indicates more red and blue tones than brighter green, these regions still show properties of edge states.

3.2.3. Description of Edge Defects

In our models, we introduced defects only for edge atoms. Figure 3.11 is one of the example configurations of the central region where the edge atoms are represented with blue and red colors. According to the figure, the defect depth is taken as one atom, also indicated in the grey region.

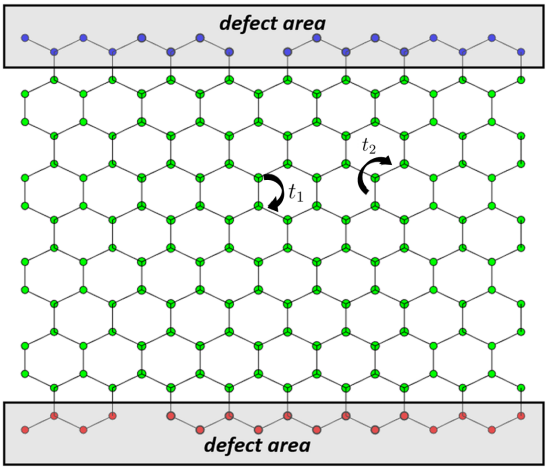

Figure 3.11. The example of the central region consists of the hexagonal structure after introducing the edge disorder where t_1 and t_2 indicate first and second nearest neighbor interaction terms.

After that, we determined a specific defect density. Defect density is the ratio of removed atoms to the total number of atoms at the edges for the pristine case.

During our calculations, we took the defect density as 20 percent, which means that two atoms were removed for every ten edge atoms. The number of removed atoms is distributed equally for both edges. After that, 1500 random disorder configurations of graphene and quartic nanoribbons were obtained for transport calculations.

3.2.4. Transport Properties of Graphene Nanoribbons

In this part, we followed the same steps as in the previous section while studying our toy model. First, we calculated the average transmission over 1500 different disorder configurations using Green's function method. Then, we used the generalized transmission equation for diffusion to determine α values and investigated the diffusion types. We performed our calculations at four different energy levels, each consisting of a different number of modes.

Figure 3.12 shows the relation between the average transmission and the system length under %20 defect density. The maximum values of the y-axis for each figure indicate the total number of modes for pristine structures at that energy. For each case, the transmission decreased with length after introducing the edge defects to the systems. The black lines are obtained from the transmission formula in Equation 1.11, where α is a fixed parameter and equals 2. This equation indicates normal diffusion and is not suitable for these data sets. Colored lines, on the other hand, indicate a fit where α and spread length λ_{sp} are taken as free parameters. At the Figures 3.12.b.,3.12.c., and 3.12.d., α values are obtained as $1.15, 0.76$ and 0.85 respectively. Since they are less than 2, each of them indicates anomalous diffusion. In addition to these three energy, we investigated one more energy at $1.09eV$, where α is 1.81 and close to 2. At this energy, α is still in the range of anomalous diffusion; however, it is very close to normal diffusion behavior. Working with this energy provides a way to compare the effects of the magnitude of α on transport for the same material. Figures also show that in the graphene nanoribbons, the spread lengths λ_{sp} increase with the number of modes. Because of that, higher energies have more data points, and working with these energies is much easier.

Furthermore, we also added error bars on data points to consider the spread in the numerical data by using standard deviation. The results in Figure 3.12 belong to the average of 1500 disorder configurations. We also repeated our calculations with larger ensemble sizes. However, results still show deviations in the same range.

Therefore, we conclude that the ensemble size is large enough. Deviations have a physical origin, which will be explained in the next section using the mode-matching method.

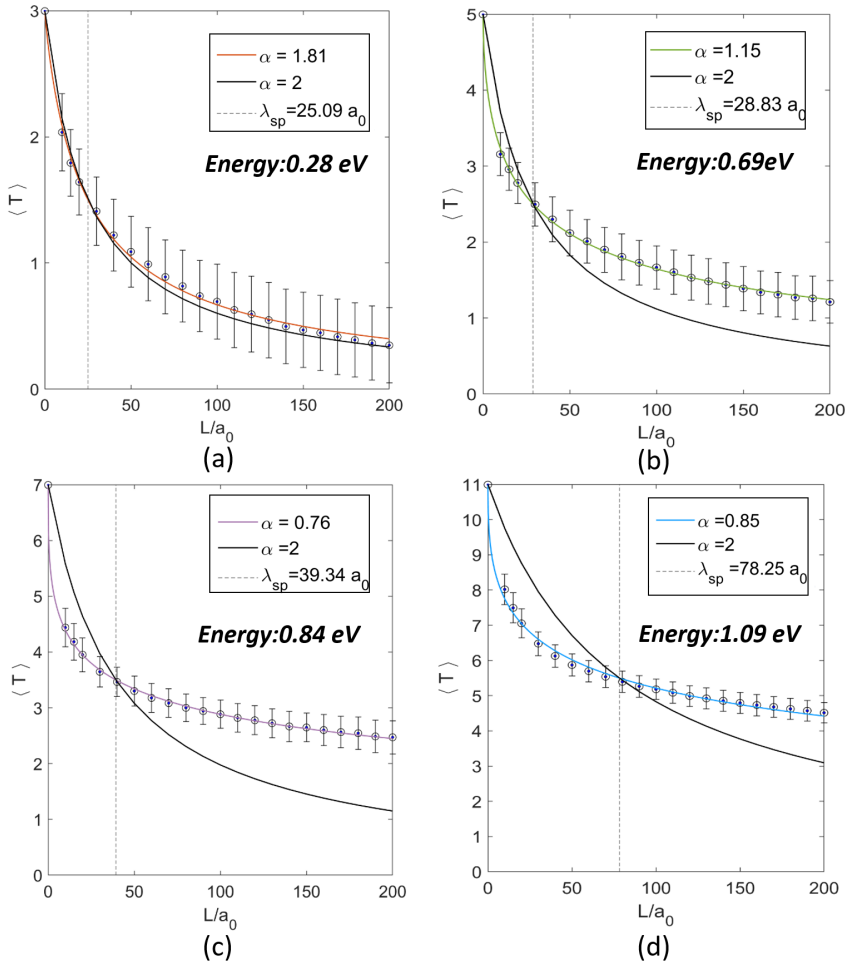

Figure 3.12. The average transmission-length relation for 12-zGNR under %20 defect density over 1500 different disorder configurations at (a)$E = 0.28eV$ (b)$E = 0.69eV$ (c)$E = 0.84eV$ (d)$E = 1.09eV$. The spread in the numerical data is calculated by using standard deviation.

Then, we investigated the relation between the resistance and the system length for these energy levels. We obtained the resistance values from the transmission data using the four-probe equation, which is

$$R_4 = \frac{1}{T} - \frac{1}{M}. \tag{3.7}$$

Here, M indicates the number of modes in the pristine system for a specific energy.

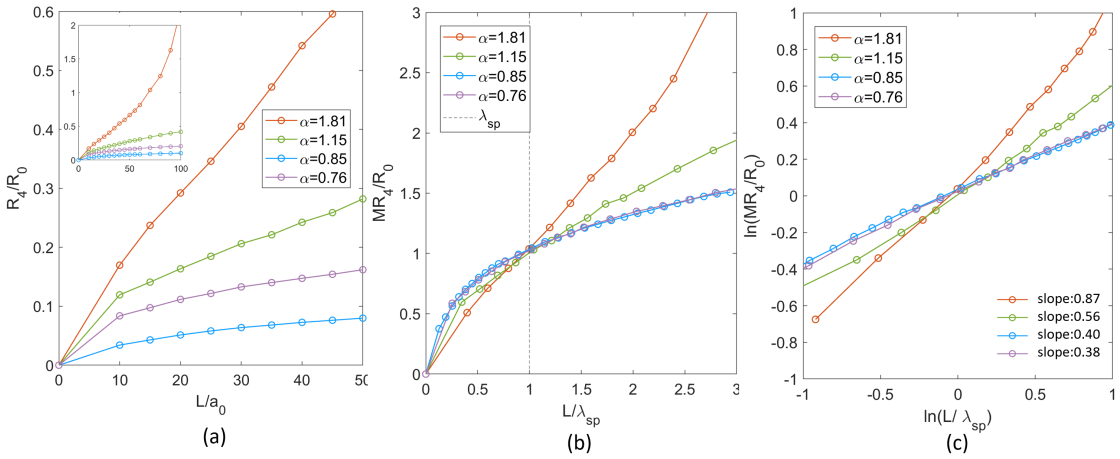

Figure 3.13. The resistance-length relation for 12-zQNR under %20 defect density over 1500 different disorder configurations for (a) the mode-dependent version (b) the mode-independent version (c) the logarithmic version.

Figure 3.13 shows the change in resistance depending on α values. In Figure 3.13.a., the resistance increases with length non-linearly while the system shows anomalous diffusion. These results are similar to the two-channel model results in the previous section. In the toy model calculations, we only observed the linear dependency between the resistance and the system length for normal diffusion. Since, this time, all α values are less than 2, we observed non-linearity for all cases. Except at the energy $0.28eV$, since α is closer to 2, the sub-linearity is not stronger like other cases but still does not indicate a straight line. In Figure 3.13.b, we multiplied the y-axis with M, and resistances become independent from the number of modes. It allows us to study four different energies at the same scale. Furthermore, we took the x-axis in terms of the L/λ_{sp}. By doing that, we aim to make clear the critical point where $L = \lambda_{sp}$. At that point, without showing dependency on the magnitude of α, all resistances become 1. Figure 3.13.c indicates the logarithmic version of the values in 3.13.b. Here, we focused on the slope of the data set. From the four-probe resistance equation, we know that the ratio of two axes in the logarithmic form gives $\alpha/2$, which indicates the slope of the figures. These results show that the slope decreases with α while the anomaly increases. After observing the anomalies, we focus on the reason behind this behavior.

In the examples from the literature, these anomalous diffusion behaviors were observed thanks to the Levy distribution. Although we did not introduce any Levy distribution in our models, we still observed anomalous behavior. To understand the reason behind that, we utilized the mode-matching method. This method provides the calculation of transmission probabilities for each mode individually.

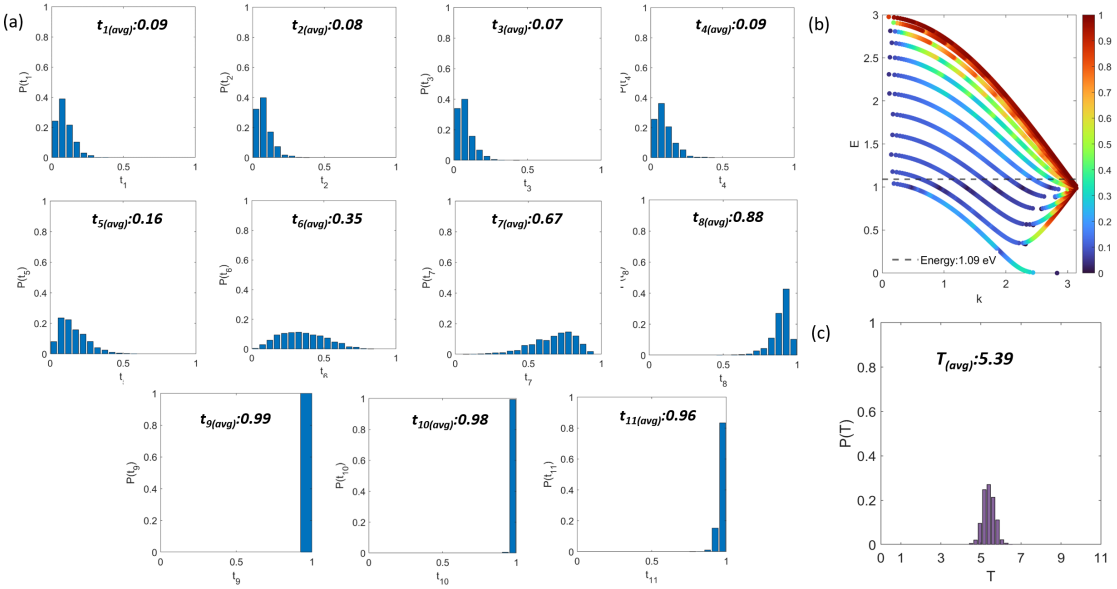

Figure 3.14. (a) The distribution of the transmission probabilities for each mode at $1.09eV$ and $L = 80a_0$ (b) The band-resolved probabilities of 12-zGNR where $L = 80a_0$ c)The total transmission probability distribution a $1.09eV$ for 12-zGNR

Figure 3.14. a shows the transmission distributions of each mode at $1.09eV$ over 1500 different disorder configurations. These calculations were performed at $L = 80a_0$, nearly equal to the spread length at that energy. According to our results, the average transmission probability changes for these modes between 0.07-0.99, indicating a wide range. This range indicates that modes can be found in different regimes simultaneously, which is the origin of the anomalous diffusion in our systems. The results in 3.14.b are also obtained from the mode-matching method and provide a visual perspective. Here, the magnitudes of the transmission probabilities of each mode can be seen for all energy levels. The color codes are defined from blue to red with an increasing transmission probability. The energy band corresponds to $1.09eV$,

indicated with a dashed line. At $1.09eV$, there are 11 modes including 3 red, 1 yellow, 1 green and 6 blue colors. The red modes are closer to the ballistic regime, while the blue modes have already entered the localization regime. Figure 3.14.c, on the other hand, shows the results obtained from Green's function method and indicates the distribution of the total transmission. This time, the x-axis changes from zero to eleven since the total number of modes at that energy is eleven. Furthermore, the mean of the distribution is equal to 5.39, which indicates the average transmission at $1.09eV$. This result also equals the sum of the average of the eleven modes in Figure 3.14.a, obtained from the Green's function method.

These results also show that the deviations in the average transmission data shown in Figure 3.12 are inevitable. Because in these models, modes of the same energy can be simultaneously found in different transport regimes. The transmission is linearly dependent on length in the diffusion regime, while in the localization regime, this relation becomes exponential.

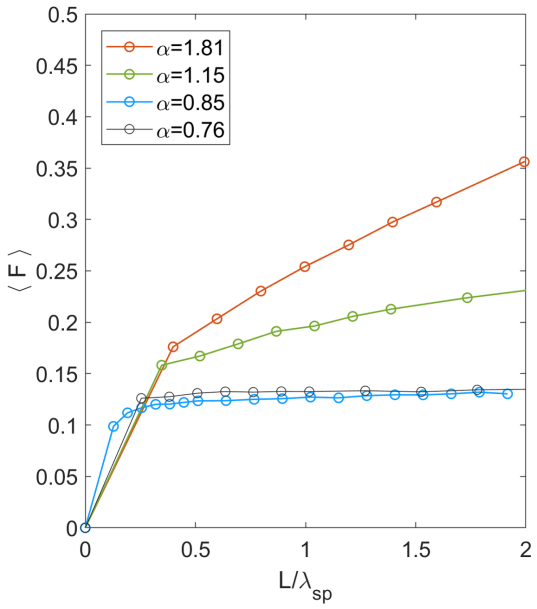

Figure 3.15. The average Fano factor- length relation at different α values for 12-zGNR.

Lastly, we investigate the Fano factor relation with an increasing length for each α value. Since it is a physically measurable term, it can be used as an indicator and gives a clue as to how the signs of the anomalies are observed experimentally.

First, we calculated the transmission matrix product ($tt^\dagger$) to determine the Fano factor. The t matrix indicates the transmission obtained from the mode matching method, and $t^\dagger$ is the Hermitian conjugate of this matrix. After calculating the eigenvalues of the product matrix, by using equation 1.40, we determined the Fano factors for each energy level. Figure 3.15 shows that the Fano factor increases faster with an increasing α. For the results where $\alpha = 1.81$ and $\alpha = 1.15$, this increases saturated near 0.2.

Studying more than two modes makes an analysis much more complex. All eigenvalues can change differently with length. From the previous mode calculations, we know that, at that energy, there are 3 red modes closer to the ballistic regime while 6 blue modes already enter the localization regime. Because of this diversity, the change in the Fano factor can not be seen easily, as in the two-channel model.

3.2.5. Transport Properties of Quartic Nanoribbons

The quartic nanoribbons have a similar hexagonal structure to graphene nanoribbons with different hopping strength ratios t_2/t_1. This ratio changes the band structure, resulting in the material gaining specific electronic properties. While constructing the tight-binding Hamiltonian, taking $t_2/t_1 > 1/6$, the quartic materials can be modeled. In our calculations, we took this ratio as 1/5.

In this part, we choose several energy levels with different numbers of modes and investigate the diffusion types at these energies. Figure 3.16 shows the average transmission system length relation under %20 defect density.The maximum values of the y-axis for each figure indicate the total number of modes for pristine structures at that energy. According to the results, the average transmission decreases with the length after introducing the edge defects. After calculating the average transmission values by using the generalized transmission equation for diffusion, we obtained α and spread length λ_{sp} at these energies. During the fitting we took them as free parameters.

Figure 3.16 shows the colored fitting curves. According to these results, α values were determined as 1.14,1.03, and 0.90 at the energies -0.63eV, -0.59 eV, and -0.51 eV, respectively. Since, in the figure, all α values are less than 2, we determined that the quartic nanoribbon shows anomalous diffusion at these energies.

Furthermore, the characteristic heavy tail behavior of the anomalous diffusion can also be observed from the fits. On the other hand, the black curves in the figures indicate the normal diffusion curves where α is taken as 2. When we compare the black curve, indicating normal diffusion, and the colored fitted curves belonging to anomalous diffusion, we can observe that data points are more suitable for anomalous diffusion. These results show that using the generalized transmission equation for diffusion is a more convenient way for our models.

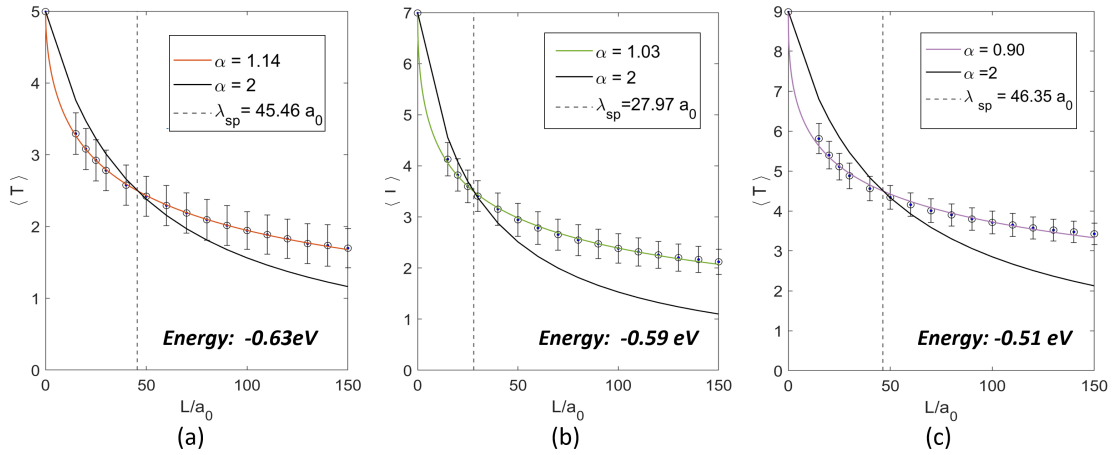

Figure 3.16. The average transmission-length relation for 12-zQNR under %20 defect density over 1500 different disorder configurations at (a)E = -0.63 eV (b)E = -0.59 eV (c)E = -0.51 eV. The spread in the numerical data is calculated by using standard deviation.

Moreover, for quartic nanoribbons, the chosen energy values and the α values at these energies are much closer when comparing the graphene nanoribbons. Since they enter localization faster, they have short spread lengths. Therefore, it is difficult to obtain enough data points, especially at lower energies.

The error bars on data points show the spread in the numerical data and are calculated using standard deviation by following the same steps in the graphene nanoribbon calculations. The origin of this behavior is based on the multichannel structure of the nanoribbons and is revealed by using the mode-matching method.

After that, we obtained resistance values from the four-probe equation in terms of the transmission. Figure 3.17. a shows the relation between the resistance and the system length at three different energy levels. Since α values in the figures

are less than 2, we can easily observe the non-linearity for these energy levels. From the two-channel model calculations, we know that this sublinear behavior resulted from the anomalies in the diffusion regime. Figure 3.17.b shows mode-independent results for resistance. The dashed line in the figure determines the critical point where the system length equals the spread length of each energy. At that point, all resistance values coincide near 1. Figure 4.17.c, on the other hand, is the logarithmic version of the results in 3.17.b. In this part, we calculated the slopes of the figures, which gives $\alpha/2$. The results show that the slopes increase with α.

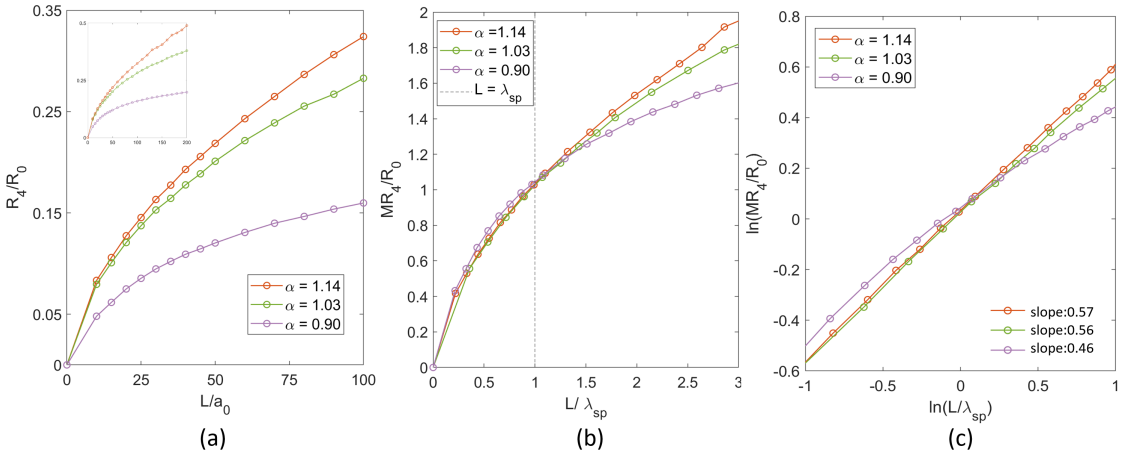

Figure 3.17. The resistance-length relation for 12-zQNR under %20 defect density over 1500 different disorder configurations for (a) the mode-dependent version (b) the mode-independent version (c) the logarithmic version.

After observing the anomalous diffusion in quartic nanoribbons, we utilized the mode-matching method for detailed analysis. In this part, we choose the energy $-0.51eV$, where $L = 50a_0$ to analyze the individual transmission properties. At that energy, 9 modes are obtained, which is less than the example in the graphene calculations. However, it is still larger when compared to the toy model. At this energy, the average transmission of the modes changes from 0.15 to 0.99, including a broad range similar to graphene nanoribbon results. Because for both systems, the origin of the anomalies comes from the multichannel mechanism where channels can enter different regimes simultaneously. Figure 3.18.b gives a visual perspective for transmission probabilities obtained using color codes. This method provides a way to simultaneously see the transmission probabilities for all energy values.

The results are in Figure 3.18.c comes from the Green's function calculation and shows the distribution of the total transmission at $-0.51eV$. The maximum value of the x-axis shows that the total number of modes equals nine at that energy. Furthermore, the mean of the distribution is equal to 4.34, which indicates the average transmission at -0.51 eV. This result also equals the sum of the average of the nine modes in Figure 3.18.a, obtained from the Green's function method.

textcolorblueThese results can be used to explain the spread in the transmission data in Figure 3.16. Since the modes at a specific energy can be found simultaneously in different regimes, the transmission length dependence will change depending on the transport regime. It will be linear in the diffusion regime, while in the localization regime, it becomes exponential.

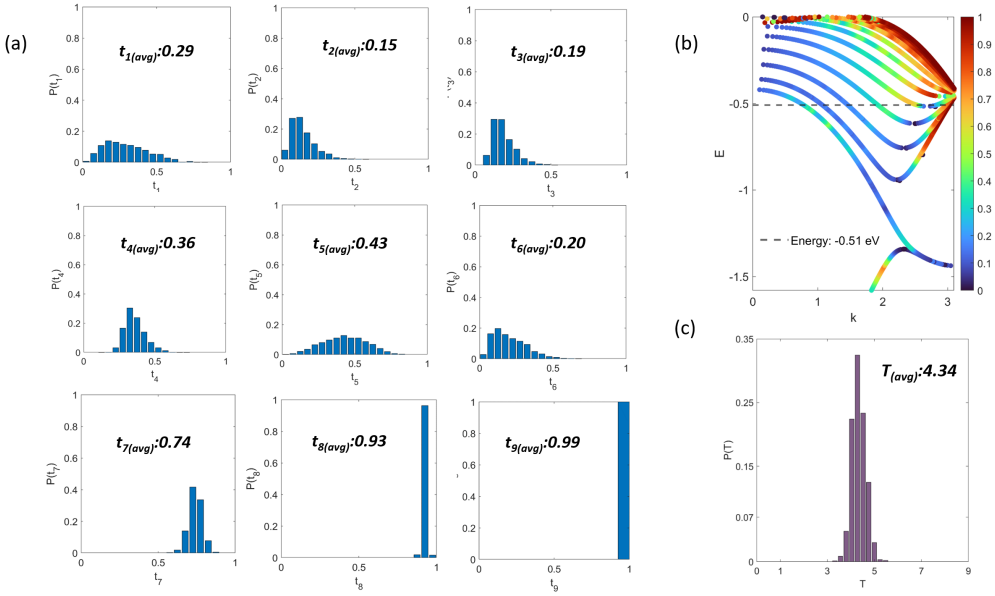

Figure 3.18. (a) The distribution of the transmission probabilities for each mode at $-0.51eV$ and $L = 50a_0$ (b) The band-resolved probabilities of 12-zQNR where $L = 50a_0$ c)The total transmission probability distribution a $-0.51eV$ for 12-zQNR.

As a final step, using the transmission matrix t, obtained from the mode matching method, we calculated the transmission matrix product $tt^{\dagger}$ and its eigenvalues. These eigenvalues are also called the transmission eigenvalues, and the Fano factor can be calculated using them. Because of that, they have an essential role in understanding the transport properties of the system. Figure 3.19 shows the average Fano

factor results with an increasing length for the energy levels at $-0.63eV, -0.59eV$, and $-0.51eV$. The number of the channels is $5, 7$ and 9, and the α values for these channels are $1.14, 1.03, 0.90$, respectively. Since the system shows anomalous diffusion at these energies, we observed non-monotonic increases at the average Fano factor depending on length.

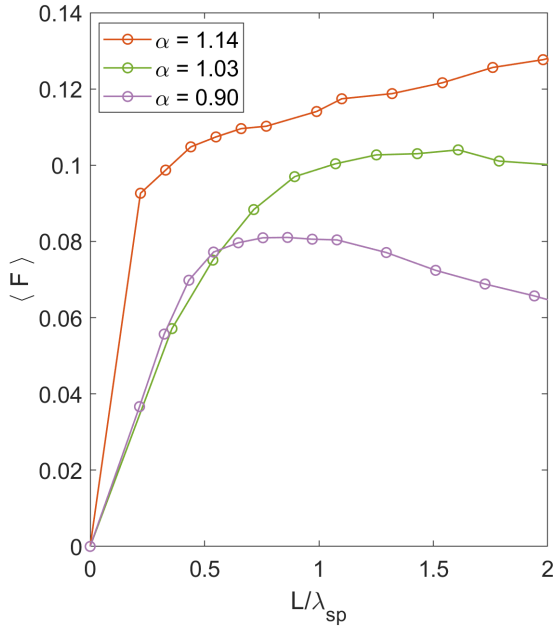

Figure 3.19. The average Fano factor- length relation at different α values for 12-zQNR.

3.3. Localization Regime

In this section, we investigated whether there is a link between the localization and diffusion regime. We introduced edge disorder with %20 defect density and performed our calculations at larger nanoribbons. In order to speed up our calculations, we used the decimation method by applying the iteration. This method is convenient for studying larger systems without constructing a total Hamiltonian.

In the literature, there are several studies related to anomalous localization (Méndez-Bermúdez et al., 2016; Amanatidis et al., 2017; Fernández-Marín et al., 2012). Their origin is based on the Levy-type disorder, similar to the studies on

anomalous diffusion. The type of localization can be determined from the relation between the geometric average of the transmission and the system length. According to the results of these studies, the geometric average of the transmission and the system length show power law dependency, which indicates anomalous localization.

According to Figure 3.20, as a common point for graphene and quartic nanoribbon, the relation between the geometric average of the transmission decreases with length linearly, which indicates normal localization. This behavior is consistent with our previous results in the diffusion regime because the effects of the multichannel mechanism are suppressed in large systems. Since anomalies resulted from the multichannel structure in our models, we did not observe this anomaly in the localization regime.

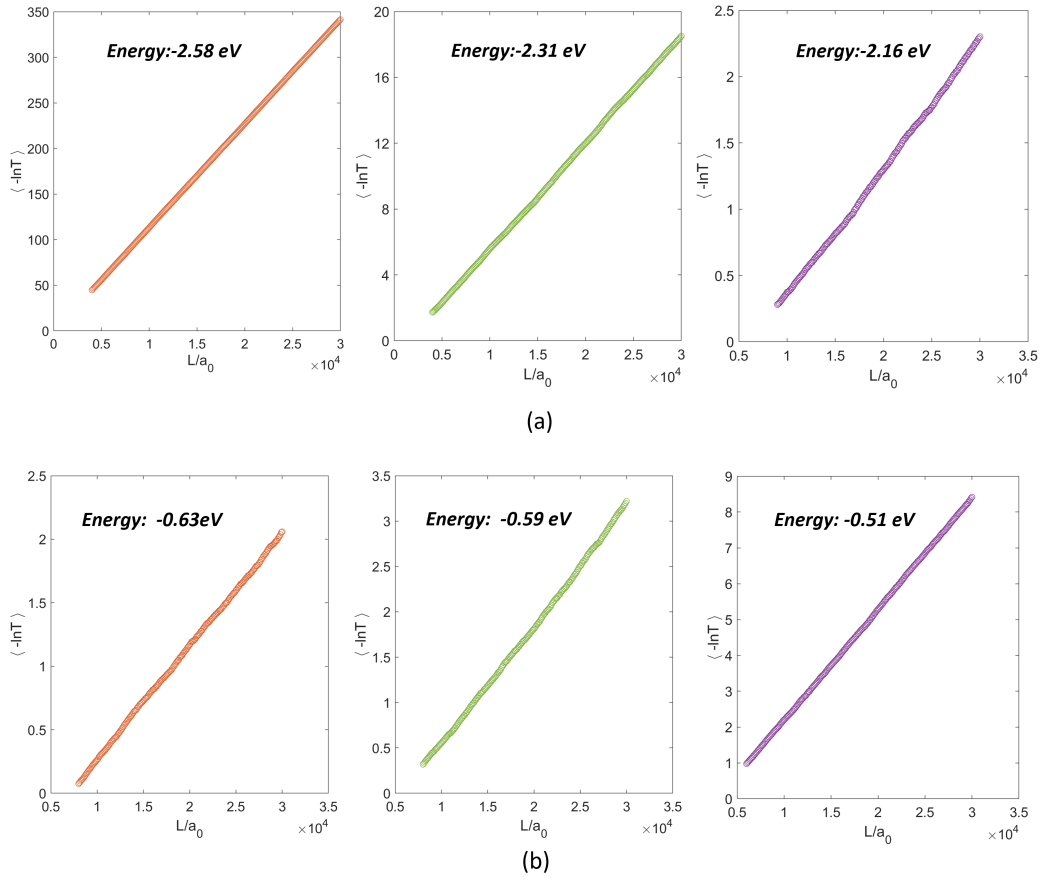

Figure 3.20. The geometric average of the transmission with respect to system length for (a)12-zGNR (b)12-zQNR.

CHAPTER 4

CONCLUSION

In this study, we investigate the anomalous quantum transport behavior in multichannel systems. While doing that, we utilized the graphene and quartic nanoribbons under edge disorder.

During our calculation, we used two main methods. From Green's function method, we calculated the electronic transmission probabilities of the systems. After obtaining the average transmission values over large ensemble sizes, we determined the α values and diffusion types using the generalized transmission equation for the diffusion regime. In addition to that, we utilized the mode matching method. This method gave us a new perspective by providing information on the transmission probabilities for each mode individually, which is essential, especially when working on multichannel systems.

Before studying nanoribbons, we constructed a basic two-channel system as a toy model to understand the characteristic properties of anomalous diffusion. Here, we followed two critical steps. The first step is introducing different Anderson disorder strengths for channels to obtain different physical properties. The other one is decreasing the ratio between the hopping strengths through the channels $t_{\parallel}$ and between the channels $t_{\perp}$. In this part, we studied two different scenarios depending on this ratio. One resulted in normal diffusion, while the other was anomalous diffusion. This model is crucial to understanding the relation between multichannel systems and anomalous transport. We can easily change the diffusion type in the same model by choosing suitable ratios. Furthermore, since we are dealing with only two channels, which is less than the modes of the nanoribbons, it is easy to follow the characteristic properties of the anomalous diffusion.

In the nanoribbon transmissions, we randomly introduced the edge defects to the systems. Both graphene and quartic nanoribbons are hexagonal structures and include more than two modes at their energy levels. The main difference is the ratio between the hopping terms, $t_2/t_1 = 0$, for graphene and $t_2/t_1 > 1/6$ for quartic nanoribbons. During our calculations, we took $t_2/t_1 = 1/5$ for quartic nanoribbons. However, the differences in this term give them characteristic behaviors during the

transport. At first sight, the mechanism underlying the anomalous behavior of nanoribbons may look different from that of the two-channel model. However, they are similar. Since defects are introduced only at edges, scattering increases only in those regions. As a result, diffusion becomes slower in the modes where the effects of the edge atoms are more dominant than the bulk atoms. In order to see these contributions on the energy band diagram, we also introduced color codes by using the probability density of the eigenvectors according to the position of the atoms in the structure. We obtained α values less than two from Green's function method, indicating anomalous diffusion for graphene and quartic nanoribbons.

After that, we investigated the behavior of the resistance with an increasing system length. From the two-channel model, we know that when the system shows normal diffusion, the relation between the four-probe resistance and system length is linear and obeys Ohm's law. On the other hand, this behavior becomes sublinear in the anomalous diffusion. In our results, we observed this sublinearity for both graphene and quartic nanoribbons.

In order to investigate the role of the correlated disorder on anomalous diffusion behavior, we utilized the mode-matching method. We obtained band-resolved probabilities and transmission distributions of each mode from this method. According to our results, the maximum and the minimum values of the average transmission probability for modes changing between $.0.07 - 0.99$ at the energy $1.09eV$ for graphene and between $0.15 - 0.99$ at $-0.51eV$ for the quartic nanoribbon. These values give information about the transport regime of the modes. They can change between 1 and 0 while indicating ballistic and localization regimes, respectively. Since the average transmission probabilities vary in a broad range in our results, it indicates the modes are in different regimes simultaneously.

After investigating anomalous diffusion behavior theoretically, we calculated the Fano factors for our systems. Since the Fano factor is a physical and measurable parameter, it is a crucial concept for our calculations. This concept provides a way to determine whether the system has an anomaly from experimental results. In order to calculate the Fano factor, we used the eigenvalues of the transmission product matrix $tt^{\dagger}$. According to our results, the Fano factor increases with length for the single-channel and two-channel systems in the case of normal diffusion. However, in the anomalous diffusion case, this behavior became nonmonotonic. While working on the two-channel model, it is much easier to see the effects of the anomalies on the Fano factor since there are only two eigenvalues. For the nanoribbons, on the other

hand, the transmission analysis becomes more complex. Because these systems have more than two eigenvalues, and their magnitudes change in a broad range. However, we can still observe the nonmonotonic increase for quartic nanoribbons and the decrease in the increment for the graphene nanoribbons.

As a final step, we investigated whether there is a link between the diffusion and localization regimes in the anomalous transport. In this part, we used the decimation method to gain speed and memory during calculations. After we obtained the geometric average of the transmission, we plotted data points with an increasing system length. According to our results, there is always a linear relation between the geometric average of the transmission and system length in all our cases. The literature shows that this linearity is a sign of standard localization.

In the literature, there are a variety of studies related to anomalous diffusion and localization (Méndez-Bermúdez et al., 2016; Amanatidis et al., 2017; Fernández-Marín et al., 2012; Zakeri et al., 2015).However, the anomalies in these systems are generally resulting from Levy distributions. Some studies introduced Levy distributions to the systems via disorders, and others used magnetic field or spin-orbit effects. On the other hand, we did not introduce any Levy distribution or applied physical concepts similar to the literature during this study. However, we still observed anomalous behavior in the diffusion regime. The literature also mentions the anomalies in the localization regime. However, in our models, we did not observe anomalous behavior at large scales. Because, at large scales, the effects of the multichannel mechanism are suppressed. This result also confirms that the origin of the anomaly in our systems resulted from the multichannel structure.

REFERENCES

Abrahams, E. 2010. *50 years of Anderson Localization*, Volume 24. world scientific.

Amanatidis, I., I. Kleftogiannis, F. Falceto, and V. A. Gopar 2017. Coherent wave transmission in quasi-one-dimensional systems with lévy disorder. *Physical Review E 96*(6), 062141.

Anderson, P. 2010. 50 years of anderson localization. *50 Years Of Anderson Localization. Edited by PW Anderson. Published by World Scientific Publishing Co. Pte. Ltd.*

Baronchelli, A. and F. Radicchi 2013. Lévy flights in human behavior and cognition. *Chaos, Solitons Fractals 56*, 101–105.

Barone, V., O. Hod, and G. E. Scuseria 2006. Electronic structure and stability of semiconducting graphene nanoribbons. *Nano letters 6*(12), 2748–2754.

Barthelemy, P., J. Bertolotti, and D. S. Wiersma 2008. A lévy flight for light. *Nature 453*(7194), 495–498.

Beenakker, C. W. 1997. Random-matrix theory of quantum transport. *Reviews of modern physics 69*(3), 731.

Blanter, Y. M. and M. Büttiker 2000. Shot noise in mesoscopic conductors. *Physics reports 336*(1-2), 1–166.

Brockmann, D., L. Hufnagel, and T. Geisel 2006. The scaling laws of human travel. *Nature 439*(7075), 462–465.

Brown, R. 1828. *A brief account of microscopical observations on the particles contained in the pollen of plants; and on the general existence of active molecules in organic and inorganic bodies*. Richard Taylor.

Buldyrev, S. V., S. Havlin, A. Y. Kazakov, M. G. da Luz, E. P. Raposo, H. E.

Stanley, and G. M. Viswanathan 2001. Average time spent by lévy flights and walks on an interval with absorbing boundaries. *Physical Review E 64*(4), 041108.

Büttiker, M. 1986. Four-terminal phase-coherent conductance. *Physical review letters 57*(14), 1761.

Büttiker, M. 1990. Scattering theory of thermal and excess noise in open conductors. *Physical review letters 65*(23), 2901.

Campos-Delgado, J., Y. Kim, T. Hayashi, A. Morelos-Gómez, M. Hofmann, H. Muramatsu, M. Endo, H. Terrones, R. Shull, M. Dresselhaus. 2009. Thermal stability studies of cvd-grown graphene nanoribbons: Defect annealing and loop formation. *Chemical Physics Letters 469*(1-3), 177–182.

Çınar, M. N., G. Ö. Sargın, K. Sevim, B. Özdamar, G. Kurt, and H. Sevinçli 2021. Ballistic thermoelectric transport properties of two-dimensional group iii-vi monolayers. *Physical Review B 103*(16), 165422.

Das, D. and H. Rahaman 2017. *Carbon nanotube and graphene nanoribbon interconnects*. CRC press.

Datta, S. 1997. *Electronic transport in mesoscopic systems*. Cambridge university press.

Datta, S. 2005. *Quantum transport: atom to transistor*. Cambridge university press.

Davis, A. and A. Marshak 1997. Lévy kinetics in slab geometry: Scaling of transmission probability. *Fractal Frontiers*, 63–72.

Einstein, A. 1956. *Investigations on the Theory of the Brownian Movement*. Courier Corporation.

Enciu, D., G. A. Nemnes, and I. Ursu 2014. Spintronic devices based on graphene nanoribbons with transition metal impurities towards space applications. *IN-*

CAS Bulletin 6(1), 45.

Fernández-Marín, A., J. Méndez-Bermúdez, and V. A. Gopar 2012. Photonic heterostructures with levy-type disorder: Statistics of coherent transmission. *Physical Review A 85*(3), 035803.

Fisher, D. S. and P. A. Lee 1981. Relation between conductivity and transmission matrix. *Physical Review B 23*(12), 6851.

Fonseca, D. B., L. F. C. Pereira, and A. L. Barbosa 2023. Lévy flight for electrons in graphene: Superdiffusive-to-diffusive transport transition. *Physical Review B 107*(15), 155432.

Iomin, A. and G. Zaslavsky 2002. Quantum manifestation of lévy-type flights in a chaotic system. *Chemical physics 284*(1-2), 3–11.

Khomyakov, P., G. Brocks, V. Karpan, M. Zwierzycki, and P. J. Kelly 2005. Conductance calculations for quantum wires and interfaces: Mode matching and greenâs functions. *Physical Review B 72*(3), 035450.

Klafter, J., G. Zumofen, and M. Shlesinger 1995. Anomalous diffusion and lévy statistics in intermittent chaotic systems. In *ChaosâThe Interplay Between Stochastic and Deterministic Behaviour: Proceedings of the XXXIst Winter School of Theoretical Physics Held in Karpacz, Poland 13–24 February 1995*, pp. 183–210. Springer.

Koenderink, A. F. and W. L. Vos 2005. Optical properties of real photonic crystals: anomalous diffuse transmission. *JOSA B 22*(5), 1075–1084.

Landauer, R. 1957. Spatial variation of currents and fields due to localized scatterers in metallic conduction. *IBM Journal of research and development 1*(3), 223–231.

Landauer, R. 1970. Electrical resistance of disordered one-dimensional lattices. *Philosophical magazine 21*(172), 863–867.

Lauritzen, S. L. 2002. *Thiele: pioneer in statistics*. Clarendon Press.

Le Thomas, N., H. Zhang, J. Jágerská, V. Zabelin, R. Houdré, I. Sagnes, and A. Talneau 2009. Light transport regimes in slow light photonic crystal waveguides. *Physical Review B 80*(12), 125332.

Leadbeater, M., V. Falko, and C. Lambert 1998. Lévy flights in quantum transport in quasiballistic wires. *Physical review letters 81*(6), 1274.

Lepri, S., S. Cavalieri, G.-L. Oppo, and D. S. Wiersma 2007. Statistical regimes of random laser fluctuations. *Physical Review A 75*(6), 063820.

Mantegna, R. N. and H. E. Stanley 1995. Scaling behaviour in the dynamics of an economic index. *Nature 376*(6535), 46–49.

Méndez-Bermúdez, J., A. Martínez-Mendoza, V. Gopar, and I. Varga 2016. Lloyd-model generalization: Conductance fluctuations in one-dimensional disordered systems. *Physical Review E 93*(1), 012135.

Miranda, L. C. and R. Riera 2001. Truncated lévy walks and an emerging market economic index. *Physica A: Statistical Mechanics and its Applications 297*(3-4), 509–520.

Nazarov, Y. V. and Y. M. Blanter 2009. *Quantum transport: introduction to nanoscience*. Cambridge university press.

Nemec, N. 2007. *Quantum transport in carbon-based nanostructures*. Ph. D. thesis.

Ong, Z.-Y. and G. Zhang 2015. Efficient approach for modeling phonon transmission probability in nanoscale interfacial thermal transport. *Physical Review B 91*(17), 174302.

Osborne, A. and R. Caponio 1990. Fractal trajectories and anomalous diffusion for chaotic particle motions in 2d turbulence. *Physical review letters 64*(15), 1733.

Özdamar, B., G. Özbal, M. N. Çınar, K. Sevim, G. Kurt, B. Kaya, and H. Sevinçli

2018. Structural, vibrational, and electronic properties of single-layer hexagonal crystals of group iv and v elements. *Physical Review B 98*(4), 045431.

Pasmanter, R. A. 1988. Anomalous diffusion and anomalous stretching in vortical flowsâ. *Fluid Dynamics Research 3*(1-4), 320–326.

Prezzi, D., D. Varsano, A. Ruini, A. Marini, and E. Molinari 2008. Optical properties of graphene nanoribbons: The role of many-body effects. *Physical Review B 77*(4), 041404.

Rocha, E. G., E. P. Santos, B. J. dos Santos, S. S. de Albuquerque, P. I. Pincheira, C. Argolo, and A. L. Moura 2020. Lévy flights for light in ordered lasers. *Physical Review A 101*(2), 023820.

Rousseau, E. and D. Felbacq 2017. Ray chaos in a photonic crystal. *Europhysics Letters 117*(1), 14002.

Ryndyk, D. A. 2016. Theory of quantum transport at nanoscale. *Springer Series in Solid-State Sciences 184*, 9.

Sancho, M. L., J. L. Sancho, J. L. Sancho, and J. Rubio 1985. Highly convergent schemes for the calculation of bulk and surface green functions. *Journal of Physics F: Metal Physics 15*(4), 851.

Schottky, W. 2018. On spontaneous current fluctuations in various electrical conductors. *Journal of Micro/Nanolithography, MEMS, and MOEMS 17*(4), 041001–041001.

Sevinçli, H. 2017. Quartic dispersion, strong singularity, magnetic instability, and unique thermoelectric properties in two-dimensional hexagonal lattices of group-va elements. *Nano Letters 17*(4), 2589–2595.

Solomon, T., E. R. Weeks, and H. L. Swinney 1994. Chaotic advection in a two-dimensional flow: Lévy flights and anomalous diffusion. *Physica D: Nonlinear Phenomena 76*(1-3), 70–84.

Torres, L. E. F., S. Roche, and J.-C. Charlier 2014. *Introduction to graphene-based nanomaterials: from electronic structure to quantum transport*. Cambridge University Press.

Uchaikin, V. V. and V. M. Zolotarev 2011. *Chance and stability: stable distributions and their applications*. Walter de Gruyter.

Van Hove, L. 1953. The occurrence of singularities in the elastic frequency distribution of a crystal. *Physical Review 89*(6), 1189.

Zakeri, S. S., S. Lepri, and D. S. Wiersma 2015. Localization in one-dimensional chains with lévy-type disorder. *Physical Review E 91*(3), 032112.

VITA

Hazan Özkan

EDUCATION

Ph.D. in Photonics Science and Engineering İzmir Institute of Technology, 2024

M.Sc. in Physics İzmir Institute of Technology, 2018

B.Sc. in Physics İzmir Institute of Technology, 2014

EMPLOYMENT

İzmir Institute of Technology, Research and Teaching Assistant, from 2019

PROJECTS

In TUBİTAK under Project No. 119F353.

"Effects of disorder and multiparticle interactions on transport in systems with quartic dispersion"

TEACHING EXPERIENCE

Assistant, PHOT110 Introduction to Programming

Assistant, PHOT222 Fundamentals of Quantum Photonics

Assistant, PHOT411 Numerical Methods in Photonics

Assistant, PHOT211 Fundamentals of Optics and Photonics Laboratory I

Assistant, PHOT499 Cooperative Education Course

Assistant, PHOT400 Summer Internship

Assistant, PHOT401 Summer Internship II

PUBLICATIONS

"Quantum transport regimes in quartic dispersion materials with Anderson disorder."
Polat, M., **Özkan, H.**, Sevinçli, H. (2024).
Journal of Applied Physics, 135(16).